

# Generation and Enhancement of Persistent Nanoscale Magnetization in All-Dielectric Metasurfaces by Optically Injected and Localized Free Carriers

Shivaksh Rawat<sup>\*,1</sup>, Samyobrata Mukherjee<sup>1</sup>, and Gennady Shvets<sup>\*,1</sup>

<sup>1</sup>School of Applied and Engineering Physics, Cornell University, Ithaca, NY 14850, USA

<sup>\*</sup>Email: sr939@cornell.edu, gshvets@cornell.edu

## Abstract

Time-varying dielectric metasurfaces supporting sharp optical resonances with a non-trivial electromagnetic field distribution represent a unique platform for realizing temporal interfaces for metasurface guided waves (MGWs). Rapidly changing metasurface resonance enables frequency conversion and temporal scattering of a concurrently propagating MGW. Using analytical methods and electromagnetic simulations, we demonstrate that localized free-carrier generation can be engineered to produce frequency-shifted, time-refracted, and reflected infrared MGWs. Furthermore, we demonstrate that such time interfaces can be utilized to generate large, highly localized quasistatic magnetic fields within the metasurfaces. The resulting nanoscale magnetization, supported by the residual circulating currents, persists after the departure of the time-scattered MGWs. We further demonstrate that the initial electromagnetic energy of the injected MGWs is partitioned between the time-reflected/refracted MGWs, residual motion of the free carriers, and a quasistatic magnetic field.

## 1 Introduction

Time-varying media have been widely studied in plasma physics for several decades. The theory of frequency upshifting (or PA) [1, 2] and spectral broadening[3] of an electromagnetic pulse was originally introduced using gaseous plasmas. Rapid free carrier (FC) generation by a laser pulse via photoionization upshifts the pulse's frequency[1, 4, 5]. Recent research has focused on time-varying optical media, offering a new platform for studying phenomena such as PA[6, 7, 8, 9], wave amplification using photonic time crystals[10, 11], negative wave extinction[12], antireflection temporal coatings[13], phase conjugation and negative refraction[14], temporal inverse prism[15], surface wave control using time interfaces (TIs)[16, 17, 18], double-slit time diffraction[19], and coherent wave control using photonic time interfaces[20, 21], among others. We refer the reader to the review article in Ref. [22] for a comprehensive overview of time-varying photonics.

One of the many interesting applications of time-varying photonics is on-demand up/down conversion of the incident frequency, with potential applications in optical signal processing and communications. Lately, the large optical near-field amplification found in doped transparent conducting oxides (TCOs) has been used to enhance light-matter interactions[23, 24, 25]. Intense pump pulse incidence on a TCO leads to temperature modulation of the electrons in the conduction band, which in turn affects the plasma frequency  $\omega_p$ , and has allowed for tunable redshifting of the probe pulse[25, 8]. Dynamic tuning of the probe frequency with selective blue- or red-shifting has been observed with two-color (UV and IR) excitation in an AZO thin film [26]. However, the need for two pump pulses at different frequencies renders this frequency-shifting scheme complex and difficult to implement. Moreover, these approaches rely on coupling the probe wavelength to the epsilon-near-zero (ENZ) mode of the substrate, constraining the accessible spectral range as a function of doping and geometric parameters, which cannot be tuned dynamically during operation. Furthermore, a significant drawback of TCOs is their extremely lossy nature in the ENZ regime, where they are typically operated [23].

We propose resonance frequency tuning of a metasurface as a platform for the realization of a time interface in a structured optical medium. Backed by numerical simulations and analytic perturbation theory, we demonstrate tunable red- and blueshifting of the metasurface resonance using localized free

carrier generation by a pump laser beam in a hot spot at each meta-atom. Manipulation of the local FC population affects the permittivity of the material constituting the metasurface and allows for tunable red-/blueshifting of the metasurface resonance. We employ this resonance-shifting mechanism as a tool to create a TI for a mid-IR (MIR) metasurface-guided wave (MGW). The MGW is a transversely confined metasurface mode that propagates along the metasurface and does not leak into the air above or the dielectric substrate below the metasurface. A sharp TI may be created if the local FC generation occurs on a time scale shorter than the optical cycle of the MGW. Such rapid FC generation may be obtained using an ultrafast pump pulse, and we employ the Keldysh multiphoton ionization model to simulate this pump-driven FC generation in Ge [27, 28]. Furthermore, we investigate the energy dynamics of the propagating MGW across the TI. We find that after the TI, the electromagnetic energy of the MGW is divided between the electromagnetic energy of the time-refracted and time-reflected waves, the kinetic energy of the free carriers, and the magnetic energy in a quasistatic magnetic field created in the hot spot by the TI.

The FCs generated in the hot spot during the TI are accelerated by the electromagnetic fields of the MGW, resulting in the formation of quasistatic currents, which circulate inside the hot spot. These quasistatic currents are set up during the TI and persist after it. The resonantly enhanced time-varying AC magnetic field of the MGW is efficiently rectified, and we obtain a quasistatic magnetic field that is localized in the hot spot. Electro-optic rectification is the generation of a zero-frequency quasistatic electric field from a time-varying electric field with frequency  $\omega$ , and has been used in the generation of laser-driven terahertz sources [29, 30]. However, electro-optic rectification is restricted to a limited set of materials, since it is dependent on nonlinear properties, which are typically weak in most optical materials. Here, we propose the efficient rectification of propagating AC magnetic fields using a time interface created by localized FC generation in an all-dielectric metasurface, which is agnostic to the nonlinear properties of the constituent materials. The rectification of AC magnetic fields from a propagating electromagnetic wave has been studied in the context of a uniform plasma [31]. However, to the best of our knowledge, this is the first proposal of the use of a TI in the rectification of an AC magnetic field to generate a persistent quasistatic magnetic field that leverages the resonant enhancement provided by a nanostructured metasurface and is dependent on the three-dimensional optical fields of the MGW and the hot spot. Nanostructured three-dimensional magnetic fields have potential applications in spintronics and computing [32]. Photonics-based approaches have been attempted to create such three-dimensional nanostructured magnetic fields and include laser-assisted nanostructuring of magnetic materials [33], and the generation of magnetization in two-dimensional materials using strong optical fields [34]. We propose a novel approach to obtaining nanostructured, three-dimensional, quasistatic magnetic fields using the rectification of the AC fields of an electromagnetic wave propagating along a metasurface at a time interface.

The rest of the manuscript is organized as follows. An all-dielectric metasurface (semiconductor meta-atoms atop an infrared transparent substrate) that will be used throughout this work as a platform to demonstrate a TI is described in Section 2. A specific metasurface design supporting high-quality factor MIR resonances and highly localized "hot spots" of the electric field intensity that can be used for localized free carrier generation (LFCG) is described in Sect. 2.2.1. Several perturbative techniques for calculating resonance frequency shifts of the metasurface due to LFCG inside the hot spots are described in Sect. 2.2.2, with the emphasis on deriving rigorous analytic expressions for the frequency shift that take into account the vectorial nature of the electromagnetic fields inside meta-atoms. We demonstrate that by controlling the density and spatial location of the generated carriers, either red- or blue-shifting of a metasurface resonance can be accomplished. Specific examples of resonance frequency modification via LFCG in a germanium-based metasurface are presented in Sect. 2.2.3. In Sect. 3.3.1, we detail our approach to the modeling of laser-driven free carrier generation in a dielectric. The effects of FC generation on a dispersive Drude-Lorentz medium are described in Sect. 3.3.2 where we rigorously derive the expressions for the currents due to the newly created FCs. Furthermore, in Sect. 3.3.3 we derive an analytic expression for the total energy density in a time-varying Drude-Lorentz medium. We find that the total energy of the system remains unaffected by the FCs when they are created at rest during a TI. In Sect. 4.4.1, we demonstrate the effects of a sharp TI on a metasurface-guided MIR mode using the pump-probe approach via time-domain simulations. An ultrashort high-frequency pump pulse can produce temporal reflections via localized metallization for a lower-frequency MIR mode while also redshifting the mode. We study the energy dynamics of the MGW mode across a time interface in Sect. 4.4.2 and describe the partitioning of the MGW's energy after the TI. In Sect. 4.4.3 we describe a quasistatic magnetic field that is generated as a result of the TI via rectification of the AC magnetic fields of the propagating MGW. Our findings are summarized in Section 5.

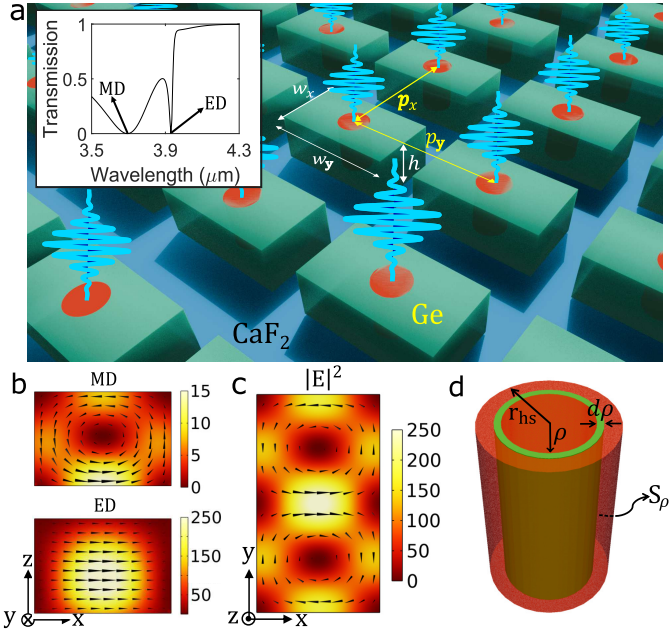


Figure 1: **a.** Schematic of a metasurface comprising rectangular semiconductor blocks periodically arranged on an infrared-transparent substrate. Red spots: cylindrical region where free carriers are generated by a laser pump. Inset: metasurface transmission spectra for normally incident  $x$ -polarized mid-infrared light. **b.** Electric field (arrows) and its intensity  $|\mathbf{E}|^2$  (color-coded) distribution at the magnetic dipolar (MD: top) and electric (ED: bottom) dipolar resonances. The field is shown in the  $x-z$  plane drawn through the middle of a meta-atom. **c.** Same as **b** for the ED resonance, but in the  $x-z$  meta-atom mid-plane. **d.** Schematic for the perturbative calculation of the resonance frequency shift produced by free-carrier generation inside the hot-spot cylinder with radius  $r_{hs}$  using annular rings (shown in green). Materials: germanium (Ge,  $n_{Ge} \approx 3.98$  [39]) for meta-atoms, calcium fluoride (CaF<sub>2</sub>,  $n_{CaF_2} \approx 1.4$  [40]) for the substrate. Geometric parameters:  $p_x = 1.94 \mu\text{m}$ ,  $p_y = 2.04 \mu\text{m}$ ,  $w_x \times w_y \times h: 0.87 \mu\text{m} \times 1.54 \mu\text{m} \times 0.6 \mu\text{m}$ , and  $r_{hs} = 200 \text{ nm}$ .

## 2 Controlling MS Optical Properties via FC Generation

The most intuitive and technically straightforward approach to rapidly changing the refractive index of a solid material is to use a laser beam to produce high densities of free electron-hole carriers. The process of free carrier generation can be further enhanced by using resonant dielectric or semiconductor metasurfaces. Nonlinear light-matter interactions inside such metasurfaces are significantly enhanced by the combination of the local field enhancement at the "hot spots" with a high-quality factor ( $Q$ ) resonance that traps light for long time periods[6, 35]. Moreover, dielectric metasurfaces have significantly higher optical damage thresholds compared to their plasmonic counterparts, which suffer higher ohmic losses [36, 37]. Thus, an all-dielectric high- $Q$  metasurface with a tunable resonance via localized free-electron generation by an intense laser pulse – including the pump-probe format, where the pump produces the carriers while the probe beam experiences the resulting change of the metasurface properties[38] – is a promising platform for temporal photonics. In the following sections, we introduce a metasurface-based approach that utilizes spatially localized free carrier generation to manipulate the spectral position of the metasurface resonance.

### 2.1 Metasurface Design

The metasurface design comprises a two-dimensional array of high-index rectangular semiconductor blocks (the meta-atoms), unequally spaced by  $p_x(y)$  in the  $x(y)$  directions on an optically transparent substrate, as shown in Fig. 1a. Note that even though the meta-atoms will be assumed to be made of the semiconductor material (e.g., germanium) for practical purposes, they will still be referred to as "all-dielectric metasurfaces" because of the nearly negligible frequency dependence of the refractive index of the constituent. We chose germanium because it offers near-zero loss and near-unity transmission in the mid-IR regime[39]. Moreover, the laser-induced damage threshold (LIDT) for germanium is extremely

large – LIDT<sub>Ge</sub>  $\sim 20.8$  mJ/cm<sup>2</sup> for subpicosecond pulses at 400 nm[38]). This makes germanium a promising candidate for ultrafast high-intensity laser applications. Furthermore, we have listed the geometric and material parameters of the metasurface in the caption of Fig. 1a. The refractive indices of the substrate and meta-atom material (CaF<sub>2</sub> and Ge, respectively) are assumed to be frequency independent for the range of mid-infrared (MIR) frequencies of the probe considered below.

The optical properties of the metasurface are shown in the inset of Fig. 1a, where the numerically calculated transmission spectrum is plotted for a range of mid-IR frequencies of interest. The two dips in the transmission spectrum correspond to the two types of resonances: a high- $Q$  ( $Q \sim 150$ ) electric dipolar resonance (marked ED at  $\lambda_{\text{ED}} \sim 3.93\mu\text{m}$ ) and a low- $Q$  ( $Q \sim 10$ ) magnetic dipolar resonance (marked MD at  $\lambda_{\text{MD}} \sim 3.69\mu\text{m}$ ). The electric/magnetic classification of the two resonances is based on the vectorial nature of the electric fields. The electric field (direction and intensity) for the MD (top) and ED (bottom) resonances in the meta-atom's  $x - z$  midplane are shown in Fig. 1b. The solenoidal nature of the electric field indicates the MD nature of the resonance at  $\lambda_{\text{MD}}$ , while the non-rotational electric field at  $\lambda_{\text{ED}}$  indicates an ED resonance.

In addition to its narrow spectral width  $\delta\omega \equiv \omega_0/Q$ , the ED resonance has a second important characteristic: a strongly enhanced and highly localized electric field intensity, as shown in Fig. 1c. As explained in Section 2.2, the amount of resonance frequency shift  $\Delta\omega$  produced by the generation of free carriers is proportional to the fraction of the energy of the electric field contained in the hot spot. Similarly, the effect of this frequency shift on the probe light stored inside the metasurface (i.e., the efficiency  $\eta$  of the TI) is proportional to the ratio of the resonance frequency shift  $\Delta\omega$  and the resonance bandwidth, i.e.,  $\eta \sim Q\Delta\omega$ . Therefore, both the high-field enhancement inside the hot spot of the resonant metasurface and its narrow bandwidth are beneficial to creating an efficient TI. Therefore, in what follows, we concentrate on the high- $Q$  ED resonance.

## 2.2 Shifting the Resonance Frequency of Spectrally-selective Metasurfaces: Perturbation Theory

In this section, we develop a general formalism to calculate the resonance frequency shift of a high- $Q$  all-dielectric metasurface using LFCG. LFCG reduces the dielectric permittivity of the constitutive material from  $\varepsilon_{\text{ini}}$  to  $\varepsilon_{\text{fin}} \equiv \varepsilon_{\text{hs}}$  in the hot spot. Two LFCG regimes will be considered: (i) the perturbative regime corresponding to a low density of the free carriers ( $\varepsilon_{\text{ini}} - \varepsilon_{\text{fin}} < \varepsilon_{\text{ini}}$ ), and (ii) the non-perturbative regime of local "metallization" corresponding to the high density of the free carriers ( $\varepsilon_{\text{fin}} \ll -\varepsilon_{\text{ini}}$ ).

Small localized modifications in the permittivity of a material inside a resonator alter its resonance frequency, and this change in resonance frequency may be understood as a perturbative effect[41, 42, 43, 44]. The early work required the knowledge of the exact perturbed electromagnetic fields (which are generally unknown) to predict this resonance shift. More recent work uses techniques borrowed from time-independent perturbation theory[45] in quantum mechanics to predict resonance frequency shifts in perturbed electromagnetic cavities [46, 47, 48, 49]. In this section, utilizing the formalism outlined in Ref. [42], we derive an equation to accurately predict fractional changes in resonance frequency for small perturbations to the meta-atom. This analytic result, which accounts for the vectorial nature of the electric field inside the perturbed hot spot of the meta-atom, is then used to accurately predict the resonance frequency shifts in the perturbative regime of low free carrier density.

We consider a perturbation arising from a localized change in permittivity due to LFCG inside a hot spot located inside a semiconductor meta-atom from an initial relative permittivity  $\varepsilon_{\text{ini}}$  to a perturbed relative permittivity  $\varepsilon_{\text{fin}}(\mathbf{r})$ , where  $\varepsilon_{\text{fin}}(\mathbf{r}) = \varepsilon_{\infty}$  outside and  $\varepsilon_{\text{fin}}(\mathbf{r}) = \varepsilon_{\text{hs}}$  inside the hot spot. The permitivity change inside the hot spot arises from changes in the free carrier density  $N_e(\mathbf{r}, t)$ :

$$\varepsilon_{\text{hs}}(\omega) = \varepsilon_{\infty} - \frac{\omega_p^2}{\omega^2 + i\Gamma\omega}; \quad \omega_p^2 = \frac{N_e e^2}{\epsilon_0 m_e}, \quad (1)$$

where  $\varepsilon_{\infty} = \varepsilon_{\text{ini}}$ ,  $m_e$  (e) are the effective mass (charge) of the free carriers,  $\epsilon_0$  is the permittivity of the vacuum, and  $\Gamma$  is the electron scattering rate. A specific example of resonance frequency shift in a Ge metasurface is described in Sec. 2.3. Following the standard perturbation theory [42, 44], we can express the resonance frequency shift  $\Delta\omega$  in terms of complex-valued and position-dependent unperturbed (and perturbed) eigenmodes' field amplitudes  $\mathbf{F}_0$  ( $\mathbf{F}'$ ), where  $\mathbf{F}$  represents the complex  $\mathbf{E}$ ,  $\mathbf{D}$ ,  $\mathbf{H}$ , and  $\mathbf{B}$  fields. The fractional shift in resonance frequency is given by

$$\frac{\text{Re}(\Delta\omega)}{\text{Re}(\omega_0)} = \frac{\int_V [(\mathbf{D}_0^* \cdot \mathbf{E}' - \mathbf{D}' \cdot \mathbf{E}_0^*) - (\mathbf{B}' \cdot \mathbf{H}_0^* - \mathbf{B}_0^* \cdot \mathbf{H}')] dV}{\int_V (\mathbf{D}' \cdot \mathbf{E}_0^* + \mathbf{B}' \cdot \mathbf{H}_0^*) dV} \quad (2)$$

where  $\omega_0$  is the resonance frequency of the unperturbed metasurface (which is complex for typically leaky metasurface resonances with the imaginary part related to the decay of the resonant fields), and  $V$  is the volume of the metasurface unit cell. Eq.(2) accurately predicts the shifts in the resonance frequency for any perturbation to the meta-atom (see Section I of the SI for details). However, it is of limited use since it requires knowledge of the complete fields in the perturbed structure, which are generally unknown.

To simplify Eq.(2) to the lowest order in the perturbed fields, we assume that the perturbed volume (hot spot) is represented by a small cylinder of radius  $r_{hs}$ , as shown in Fig. 1d, which can be broken up into infinitesimally thin annular shells with radii  $0 < \rho < r_{hs}$ , thicknesses  $d\rho$ , and area  $S_\rho$ . Equation (2) may be further simplified by decomposing the fields into normal ( $\perp$ ) and tangential ( $\parallel$ ) components with respect to the surface 'S' of the infinitesimally thin annular cylinder. Since  $\mathbf{D}_\perp$ ,  $\mathbf{E}_\parallel$ ,  $\mathbf{H}_\perp$ , and  $\mathbf{B}_\parallel$  are continuous across an interface, all the fields in eq. (2) are expressed in terms of these continuous components:  $\mathbf{D}_0 = \epsilon_0 \epsilon_{ini} \mathbf{E}_0 \parallel + \mathbf{D}_{0\perp}$ , and  $\mathbf{E}' = \mathbf{E}_\parallel + (1/\epsilon_0 \epsilon_{fin}) \mathbf{D}'_\perp$ . The second term inside the integral in the numerator of 2 vanishes because the magnetic permeability is unchanged. Furthermore, since we consider small changes in permittivity and infinitesimally thin shells, we assume that  $\mathbf{E}'_\parallel(\rho) = \mathbf{E}_0 \parallel(\rho)$  and  $\mathbf{D}'_\perp(\rho) = \mathbf{D}_{0\perp}(\rho)$  (azimuthal angle  $\phi$  dependence and the variation of fields in the  $z$  direction have been implicitly assumed). Keeping only the unperturbed fields in the denominator of Eq. 2, the following simplified expression for the frequency shift is obtained:

$$\frac{\text{Re}(\Delta\omega)}{\text{Re}(\omega_0)} = \frac{\epsilon_0}{2N} \int_0^{r_{hs}} d\rho \times \oint_{S_\rho} dS_\rho \left[ (\epsilon_{ini} - \epsilon_{fin}) |\mathbf{E}_0 \parallel|^2 + \left( \frac{1}{\epsilon_{fin}} - \frac{1}{\epsilon_{ini}} \right) |\mathbf{D}_{0\perp}|^2 \right] \quad (3)$$

where the integration volume  $V$  in the numerator of Eq. 2 has been reduced to that of the hot spot, and  $N$  is the normalization coefficient ( $N$  is also the total energy in the unperturbed metasurface unit cell at resonance):

$$N = \frac{1}{2} \int_V (\epsilon_0 \epsilon_{ini} |\mathbf{E}_0|^2 + \mu_0 |\mathbf{H}_0|^2) dV \quad (4)$$

Although eq. (3) has been derived for small changes in dielectric permittivity inside the hot spot, several crucial conclusions can be drawn from it. First, it follows that a small reduction in the dielectric permittivity of the hot spot due to LFCG blue-shifts the resonance frequency:  $\Delta\omega > 0$  if  $0 < \epsilon_{fin} < \epsilon_{ini}$ . Second, we note that the blueshift  $\Delta\omega$  is expected to be particularly large when  $\epsilon_{fin} \approx 0$ , i.e., when the hot spot material enters the epsilon-near-zero (ENZ) regime. Third, Eq. (3) indicates that the sign of  $\Delta\omega$  changes when the hot spot becomes plasmonic ( $\epsilon_{fin} < 0$ ), including the regime of complete metallization ( $\epsilon_{fin} \ll -\epsilon_{ini}$ ). The comparison between the predictions of Eq. (3) and other methods is given in the SOM.

Although the regime of complete metallization does not satisfy the conditions of small deviation of the material permittivity inside the hot spot from that of the rest of the meta-atom, it may still be possible to calculate the resonance frequency perturbatively. In fact, the original calculation of the resonance frequency shift of a perturbed microwave cavity by Slater [50] assumed the introduction of a small volume  $\Delta V$  of a perfect electric conductor (PEC) into the resonator. The resulting frequency shift  $\Delta\omega_{PEC}$  of the resonator is given by

$$\frac{\text{Re}(\Delta\omega_{PEC}^2)}{\text{Re}(\omega_0^2)} = \int_{\Delta V} \left( \mu_0 |\mathbf{H}_0|^2 - \epsilon_0 \epsilon_\infty |\mathbf{E}_0|^2 \right) dV \quad (5)$$

where the unperturbed electric and magnetic fields are normalized as:  $\int_V \mathbf{H}_0^* \cdot \mathbf{H}_0 dV = 1/\mu_0$ ;  $\int_V \mathbf{E}_0^* \cdot \mathbf{E}_0 dV = 1/\epsilon_0 \epsilon_\infty$ . Assuming a dispersion-free high-frequency relative permittivity for Ge (i.e.,  $d\epsilon_\infty/d\omega = 0$ ) and absence of free carriers ( $\omega_p = 0$ ), the choice of normalization gives the magnetic and electric energy density as  $W_m = \mu_0 |\mathbf{H}_0|^2/2$  and  $W_e = \epsilon_0 \epsilon_\infty |\mathbf{E}_0|^2/2$ , respectively. Throughout the manuscript, we treat the PEC and complete metallization states of the material inside the hot spot as interchangeable terms. Equation (5) makes specific predictions as to when the introduction of a PEC, blue/red-shifts the metasurface resonance. Now, when a PEC is introduced inside a region of the resonator where the electric energy is dominant, the integral in eq.(5) becomes negative, red-shifting the eigenfrequency. However, if the PEC is introduced in a region where the magnetic energy density is dominant, the integral becomes positive and the resonance blueshifts. Note that this formalism can only be applied to predict the shift of the metasurface resonance when a region in the Ge block is metallized due to a large localized FC density.

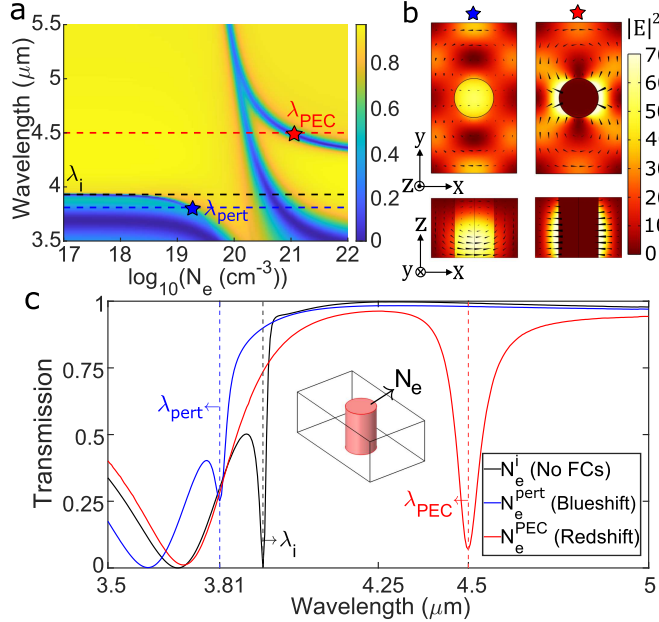


Figure 2: **a.** Metasurface transmission as a function of hot spot free carrier density ( $N_e(\mathbf{r}, t)$ ) for normally incident x-polarized light. **b.** Intensity  $|\mathbf{E}|^2$  enhancement (color), and  $\mathbf{E}$  (black cones) of the ED resonance in the meta-atom's x-y and x-z mid-planes for  $\lambda_{\text{pert}} = 3.81 \mu\text{m}$ ,  $N_e^{\text{pert}} = 1.6 \times 10^{19} \text{ cm}^{-3}$  (blue star) and  $\lambda_{\text{PEC}} = 4.5 \mu\text{m}$ ,  $N_e^{\text{PEC}} = 9.4 \times 10^{20} \text{ cm}^{-3}$  (red star) **c.** The black curve shows the metasurface transmission spectrum before FC generation ( $N_e^i = 0$ ), while the blue (red) curve shows the spectrum when the carrier density is increased to  $N_e^{\text{pert}}$  ( $N_e^{\text{PEC}}$ ). The stars and dashed lines serve as guides to the eye.

### 2.3 Example: Resonance Frequency Shifting in Ge Metasurface

Modification of the local permittivity in the Ge block provides a mechanism to tune the resonance frequency of the metasurface. The permittivity can be modified by LFCG at the hot spot (red cylinders in Ge blocks in Fig. 1a). Specifically, we consider a hot spot with radius  $r_{\text{hs}} = 200 \text{ nm}$  where the local FC density can change rapidly. The hot spot may be generated by an ultra-short high-intensity pump pulse converted into a spatial array of focused pulses using a diffractive beam splitter[51]. Alternately, the hot spot may also be created from local field enhancement under illumination by a pump pulse. Deep subwavelength spatial localization of FC generation has been achieved using mid-IR pulses in the tunneling regime (e.g., the radius of the hot spot  $r_{\text{hs}} < \lambda/40$  reported in ref.[35]). The evolution of the metasurface transmission spectrum (calculated using COMSOL Multiphysics) as the hot spot's FC density  $N_e(\mathbf{r}, t)$  increases from  $10^{17} \text{ cm}^{-3}$  to  $10^{22} \text{ cm}^{-3}$  is shown in Fig. 2a. For  $3.5 \mu\text{m} \leq \lambda \leq 5.5 \mu\text{m}$ , the permittivity in the hot spot,  $\varepsilon_{\text{hs}}$ , varies in the range  $0 < \varepsilon_{\text{fin}} = \varepsilon_{\text{hs}} < \varepsilon_{\text{ini}}$  when  $N_e \lesssim 10^{20} \text{ cm}^{-3}$ . We see in Fig. 2a that the dips in the metasurface transmission spectrum corresponding to the ED and MD resonances shift to lower values of  $\lambda$  as  $N_e$  increases from  $10^{17}$  to  $10^{20} \text{ cm}^{-3}$ . This upshifting of the resonance frequency as  $\varepsilon_{\text{fin}} = \varepsilon_{\text{hs}}$  decreases from  $\varepsilon_{\text{ini}}$  to 0 is in agreement with the prediction of eq.3. For  $N_e > 10^{20} \text{ cm}^{-3}$ , both the ED and MD resonances disappear and then reappear at much higher wavelengths, exhibiting a strong redshift. This is because for large FC density, the hot spot metallizes, strongly modifying the resonant fields. Such modifications are beyond the perturbative regime, and the resonance frequency shift can be predicted using eq.(5). Since the hot spot is located in the center of the Ge block and occupies a region of high electric energy density, eq.(5) predicts that metallizing the hot spot would cause the resonance to redshift.

The field enhancement in intensity  $|\mathbf{E}|^2$  due to the excitation of the ED resonance in the Ge block is shown in Fig. 2b for two representative cases. In the first case, marked by a blue star in Figs. 2a and b, we are in the perturbative regime with  $0 < \varepsilon_{\text{hs}} < \varepsilon_{\text{ini}}$ . Fig. 2b shows the intensity profile of the ED resonance blueshifted to  $\lambda_{\text{pert}} = 3.81 \mu\text{m}$  when  $N_e^{\text{pert}} = 1.6 \times 10^{19} \text{ cm}^{-3}$ . We choose these parameters to illustrate the perturbative case, since  $\varepsilon_{\text{hs}}(\lambda_{\text{pert}}, N_e^{\text{pert}}) \sim 10 < \varepsilon_{\infty} \sim 16$  and the ED resonance maintains a reasonably high Q-factor $\sim 48$ . The spatial profile of  $|\mathbf{E}|^2$  is quite similar to the unperturbed case when  $\varepsilon_{\text{hs}} = \varepsilon_{\text{ini}}$  (Fig. 1c). The second case, marked by a red star in Figs. 2a and b,

lies beyond the perturbative regime where  $\varepsilon_{hs} \ll 0$  and the hot spot effectively behaves like a metal. We choose the resonance at  $\lambda_{PEC} = 4.5 \mu\text{m}$  when  $N_e^{PEC} = 9.4 \times 10^{20} \text{ cm}^{-3}$  and refer to this as the PEC case ( $\varepsilon_{hs}(\lambda_{PEC}, N_e^{PEC}) \sim -400$ ). In this case, we find that the electric field has been expelled from the hot spot and the spatial profile of  $|\mathbf{E}|^2$  is strongly modified. However, it is clear from the spatial profile in the rest of the Ge block that the same ED resonance has been excited.

The transmission spectra of the metasurface for three different values of the FC density at the hot spot  $N_e(\mathbf{r}, t)$  is shown in Fig. 2c. The black curve shows the metasurface spectrum for the unperturbed case before the pump generates any FC ( $\varepsilon_{hs} = \varepsilon_{ini}$ ), with the ED resonance at  $\lambda_i = 3.93 \mu\text{m}$ . The blue curve shows the spectrum for  $N_e = N_e^{\text{pert}}$ , where we see significant blueshifting of both the ED and MD resonances. The ED resonance blueshifts to  $\lambda_{\text{pert}} = 3.81 \mu\text{m}$ . Although the  $Q$  factor of the blueshifted ED resonance decreases, it is still appreciable with  $Q_{\text{pert}} = 48$ . Upon further increasing  $N_e$  while maintaining  $\varepsilon_{hs} > 0$ , the resonance quality factors decrease and the resonances vanish completely in the regime where  $\varepsilon_{hs} = 0$ . The red curve shows the spectrum for  $N_e = N_e^{PEC}$  when the hot spot is metallized and the ED resonance redshifts significantly to  $\lambda_{PEC} = 4.5 \mu\text{m}$  with  $Q_{PEC} = 57$ . Although the MD resonance also redshifts, the effect of the metallization of the hot spot is less pronounced.

An electrostatic model that calculates the effective permittivity of the meta-atom for variable free electron densities inside the hot spot is presented in Section II of the Supplementary Information. The model qualitatively predicts the shifts in the metasurface resonance frequency when the hot spot's relative permittivity is varied between  $-\infty < \varepsilon_{hs} \leq \varepsilon_\infty$ . The model calculates the capacitance and hence the effective permittivity by assuming the hot spot as a material inclusion ( $\varepsilon_{hs}(N_e(\mathbf{r}, t))$  : relative permittivity of the inclusion) inside the capacitive meta-atom when a constant potential difference is applied across the meta-atom.

### 3 Modeling Time Interfaces in Semiconductors Using Free Carrier Generation

Locally generating FCs in the nanostructures of a metasurface allows us to dynamically tune the effective permittivity and the resonance frequency of the metasurface. This makes LFCG in an all-dielectric metasurface a promising platform for time-varying photonics at mid-IR wavelengths. To understand the optical effects of localized FC generation in the hot spot, we modeled each meta-atom as a time-varying Drude-Lorentz medium and derived the wave equation for the time-varying metasurface. Specifically, we study the impact of resonance shifting via controlled LFCG in the hot spot to theoretically demonstrate that the metasurface resonance can be tuned in less than one optical cycle of the mid-IR probe (i.e., the metasurface guided wave or MGW) via an optical pump pulse to realize a sharp TI. We study the case where localized FCG leads to a red shift of the metasurface resonance frequency and find that the MGW is also red-shifted.

#### 3.1 Laser-Induced Free Carrier Generation

Upon irradiation of an intense laser pulse on a solid, FCs are generated via photoionization (photon absorption leads to bound electrons being freed) and avalanche ionization (electrons accelerated by the laser field collide with neutral atoms and eject more electrons). We use the Keldysh model [28] to obtain the FC density in Ge,  $N_e$ , using a combined rate equation that accounts for both photoionization and avalanche ionization,

$$\frac{\partial N_e}{\partial t} = R_{PI}(I[t]) + R_{AV}(I[t])N_e - \frac{N_e}{\tau_{e-h}} \quad (6)$$

where  $\tau_{e-h}$  is the electron-hole recombination time, and a partial derivative is and will be used to explicitly calculate the time derivative while also implying a spatial dependence of the differentiated quantity. We used a pump pulse at  $\lambda_{\text{pump}} = 400 \text{ nm}$ , with a pulse width  $\tau_{\text{pump}} = 8 \text{ fs}$ , focused on the hot spot to locally generate FCs and manipulate the permittivity at the hot spot. The pump intensity incident at the hot spot is  $I[t] = I_0 \cos^2(k_{\text{pump}}z + \omega_{\text{pump}}t) e^{-2(t-\tau_1)^2/\tau_{\text{pump}}^2}$ , where  $\omega_{\text{pump}} = 2\pi c/\lambda_{\text{pump}} = k_{\text{pump}}c$  and  $\tau_1 = 3 \text{ ps}$ . The normalized pump intensity ( $I[t]/I_0$ ,  $I_0 = 2.15 \text{ TW/cm}^2$ ) and the temporal evolution of  $N_e$  in the hot spot are shown in the inset of Fig. 3a.  $\tau_{e-h}$  in Ge is on the order of hundreds of picoseconds and thus is much longer than the time period and pulse width of the optical pump and the mid-IR MGWs[52]. Therefore, the FC population in the hot spot is maintained for a sufficiently long time, and we restrict ourselves to the sharp TI between the two phases of the hot spot before and after LFCG,

i.e., the unionized phase (before the TI) and the ionized phase (after the TI). Further details on the calculation of  $N_e$  using the Keldysh model are provided in Section III of the Supplementary Information.

For the pump pulse and material parameters chosen, the photoionization rate is an order of magnitude higher than the avalanche ionization rate (see Fig. 1a in the supplementary information). The Keldysh model for ionization by an optical field accounts for both the tunneling ionization and the multiphoton absorption. For the material comprising the metasurface, Ge (band gap  $\Delta \approx 0.8$  eV and electron's reduced mass  $m_e = 0.041m_0$ ) [53], and the given pump pulse parameters (average pump intensity  $I_{avg} = 1.2$  TW/cm<sup>2</sup>), the Keldysh parameter  $\gamma_p = \omega_{pump}\sqrt{m_e\Delta}/eF \approx 0.677$  (where the average electric field strength  $F = \sqrt{2I_{avg}/c\epsilon_0}$ ) [28]. Since  $\gamma_p < 1$ , tunneling ionization is the dominant mechanism[54] and the newly formed free electrons possess negligible kinetic energy.

### 3.2 Time-Varying Dispersive Medium

We model Ge as a Drude-Lorentz dispersive medium to understand the optical effects of FC generation at the hot spot by an intense pump pulse. The displacement field  $\mathbf{D}$  and the polarization current  $\mathbf{J}_e$  in a Drude-Lorentz medium are

$$\mathbf{D} = \epsilon_0\epsilon_\infty\mathbf{E} + \mathbf{P}_e; \quad \mathbf{J}_e = \frac{\partial\mathbf{P}_e}{\partial t} \quad (7)$$

where  $\epsilon_0$  is the permittivity of vacuum,  $\epsilon_\infty$  is the response of bound electrons,  $\mathbf{E}$  is the electric field, and  $\mathbf{P}_e$  is the density of the FC-induced dipole moment. The polarization current,  $\mathbf{J}_e$ , is formed as a result of the interaction of MGW fields with FCs. We consider a medium with pre-existing free electrons whose density is  $N_e^{(1)}$  and newly created free electrons at rest whose density at any instant of time,  $t$ , is  $N_e^{(2)}(t)$  such that the total FC density in the medium is  $N_e(t) = N_e^{(1)} + N_e^{(2)}(t)$ . Under the two-fluid approximation for two different electronic populations, where we consider only the electronic motion in a neutral plasma, the polarization current density is given by

$$\begin{aligned} \mathbf{J}_e(t) &= \mathbf{J}_e^{(1)}(t) + \mathbf{J}_e^{(2)}(t) \\ &= -eN_e^{(1)}\mathbf{v}_e^{(1)}(t) - e \int_{-\infty}^t \frac{\partial N_e^{(2)}}{\partial t'} \mathbf{v}_e^{(2)}(t, t') dt' \end{aligned} \quad (8)$$

where  $\mathbf{J}_e^{(1)}$  and  $\mathbf{J}_e^{(2)}$  are the electron current densities due to the pre-existing and newly created free electrons, respectively.  $\mathbf{v}_e^{(1)}(t)$  is the velocity of a pre-existing electron, and  $\mathbf{v}_e^{(2)}(t, t')$  is the velocity at time  $t$  of an electron created at time  $t'$  (where  $t > t'$ ) [55]. These velocities, due to acceleration by the electric field of an electromagnetic wave, are calculated as

$$\begin{aligned} \mathbf{v}_e^{(1)}(t) &= -\frac{e}{m_e} \int_{-\infty}^t \mathbf{E}(t'') dt'' = \frac{e}{m_e} \mathbf{A}(t) \\ \mathbf{v}_e^{(2)}(t, t') &= -\frac{e}{m_e} \int_{t'}^t \mathbf{E}(t'') dt'' = \frac{e}{m_e} [\mathbf{A}(t) - \mathbf{A}(t')] \end{aligned} \quad (9)$$

where we have used  $\mathbf{E} = -\partial\mathbf{A}/\partial t$  to write the velocities in terms of the magnetic vector potential  $\mathbf{A}$ . The newly created free electrons that contribute to the current  $\mathbf{J}_e^{(2)}$ , are accelerated only after their creation at time  $(t')$  as seen through the integration limits for  $\mathbf{v}_e^{(2)}(t, t')$  in eq. (9). Here we neglect the nonparabolicity of the electronic bands and assume the same effective mass  $m_e$  for all electrons in the conduction band of Ge. The sum of the two polarization current densities due to the pre-existing carriers and the new carriers generated by LFCG due to the pump pulse is given as

$$\begin{aligned} \mathbf{J}_e^{(1)} + \mathbf{J}_e^{(2)} &= \frac{\partial\mathbf{P}_e}{\partial t} = -\frac{e^2 N_e^{(1)}}{m_e} \mathbf{A}(t) - \frac{e^2 N_e^{(2)}(t)}{m_e} \mathbf{A}(t) \\ &\quad + \frac{e^2}{m_e} \int_{-\infty}^t \frac{\partial N_e^{(2)}}{\partial t'} \mathbf{A}(t') dt' \end{aligned} \quad (10)$$

Calculating the first-order time derivative of  $\mathbf{J}_e$  from eq. (10), yields

$$\frac{\partial\mathbf{J}_e}{\partial t} = \frac{\partial^2\mathbf{P}_e}{\partial t^2} = \frac{e^2}{m_e} [N_e^{(1)} + N_e^{(2)}(t)] \mathbf{E} = \frac{e^2 N_e(t)}{m_e} \mathbf{E} = \epsilon_0 \omega_p^2(t) \mathbf{E} \quad (11)$$

Here, we emphasize that  $\partial \mathbf{J}_e / \partial t$  is independent of  $\partial N_e / \partial t$ . This implies that the free electrons created at time 't' do not contribute to the current density at the same instant because the electrons are created at rest. Now, starting from Ampere's law, we formulate the wave equation in terms of  $\mathbf{A}$  as

$$\nabla \times (\nabla \times \mathbf{A}) + \frac{\epsilon_\infty}{c^2} \frac{\partial^2 \mathbf{A}}{\partial t^2} - \mu_0 \frac{\partial \mathbf{P}_e}{\partial t} = 0; \quad \mathbf{H} = \frac{1}{\mu_0} (\nabla \times \mathbf{A}) \quad (12)$$

COMSOL's time domain solver uses eq. (12) in combination with eq. (11) to simulate the interaction between a MGW and FCs at the hot spot. We numerically solve eq.(6) to obtain the temporal evolution of  $N_e$  for a pump pulse and use it to model a sharp TI for the MGW. Within the TI, FCs created at rest are accelerated by the electromagnetic field, resulting in the formation of DC currents in the system. These constant currents establish a quasistatic magnetic field ( $\mathbf{H}_s$ ) and consequently a quasistatic magnetic vector potential ( $\mathbf{A}_s$ ) in the system. The quasistatic magnetic field mode (QS mode) is a zero-frequency mode, which is temporally invariant but spatially varying. After the TI ( $t > t_{TI}$ ), under the quasi-monochromatic wave approximation, we can write the total magnetic vector potential as

$$\mathbf{A}(\mathbf{r}, t) = \mathbf{A}_s(\mathbf{r}) + \mathbf{A}_t(\mathbf{r}, t) + \text{c.c.}; \quad \mathbf{A}_t(\mathbf{r}, t) = \mathbf{A}_{t0}(\mathbf{r}) e^{-i\omega_f t} \quad (13)$$

where  $\mathbf{A}_t(\mathbf{r}, t)$  denotes the amplitude of the time-varying or AC component of the magnetic vector potential and  $\omega_f$  is the frequency of the EM wave after TI. In general, for  $t > t_{TI}$ , using the ansatz above for  $\mathbf{A}(\mathbf{r}, t)$  in eqs. (10, 12), and taking only the time-independent components (see Section VI in the supplementary information), the amplitude of the QS mode at the hot spot  $\mathbf{A}(\mathbf{r})$  satisfies

$$\begin{aligned} \mathbf{H}_s(\mathbf{r}) &= \frac{1}{\mu_0} \nabla \times \mathbf{A}_s(\mathbf{r}) \\ (\omega_p^2 - c^2 \nabla^2) \mathbf{A}_s(\mathbf{r}) &= \frac{e^2}{\epsilon_0 m_e} \int_{-\infty}^t \frac{\partial N_e^{(2)}}{\partial t'} \mathbf{A}(\mathbf{r}, t') dt' \end{aligned} \quad (14)$$

The net radiation from the QS mode is zero, which corresponds to a net zero electric field ( $\mathbf{E}_s = -\partial \mathbf{A}_s / \partial t = 0$ ). This nonradiative zero-frequency mode consumes a finite fraction of the total energy of the MGW, which is stored as the energy in the DC motion of the FCs. In the next section, we study the energy dynamics in a time-varying Drude-Lorentz medium.

### 3.3 Energy Relations

In this section, starting from Poynting's theorem, we write an analytic expression for the total energy density in a time-varying Drude-Lorentz medium (derivation shown in the SI). At the TI, we numerically show, using the expression for the total energy density, that the energy in a dispersive system does not change across a time interface. During simulations, electromagnetic radiation leaks out of the simulation domain through the scattering boundaries. From Poynting's theorem, the rate of change of the total energy density can be written as (see Section V in the supplementary information)

$$\frac{\partial U}{\partial t} = -\nabla \cdot (\mathbf{E} \times \mathbf{H}) = \frac{\partial}{\partial t} \left( \frac{1}{2} \epsilon_0 \epsilon_\infty |\mathbf{E}|^2 + \frac{1}{2} \mu_0 |\mathbf{H}|^2 \right) + \mathbf{E} \cdot \frac{\partial \mathbf{P}_e}{\partial t} \quad (15)$$

For  $t > t_{TI}$ , using the expression for  $\mathbf{A}(\mathbf{r}, t)$  from eq. (13), and  $\mathbf{E}(t) = -\partial \mathbf{A} / \partial t$  in conjunction with the expressions for current given in eq. (10) in eq. (15) yields

$$-\frac{\partial U_{EM}}{\partial t} = \nabla \cdot (\mathbf{E} \times \mathbf{H}) + \mathbf{E} \cdot \mathbf{J}_{e,s} \quad (16)$$

where  $U_{EM}$  is the electromagnetic energy density, and  $\mathbf{J}_{e,s}$  is the residual or DC current in the system due to the QS mode, and are defined as

$$\begin{aligned} U_{EM} &= \frac{1}{2} \epsilon_0 \epsilon_\infty |\mathbf{E}|^2 + \frac{1}{2} \mu_0 |\mathbf{H}|^2 + \frac{1}{2} \epsilon_0 \omega_p^2(t) |\mathbf{A}_t|^2 \\ \mathbf{J}_{e,s}(\mathbf{r}) &= -\frac{e^2 N_e(t)}{m_e} \mathbf{A}_s(\mathbf{r}) + \frac{e^2}{m_e} \int_{-\infty}^t \frac{\partial N_e^{(2)}}{\partial t'} \mathbf{A}(\mathbf{r}, t') dt' \end{aligned} \quad (17)$$

From eq. (16) we observe that the rate of change of the electromagnetic energy density after the TI is equal to the sum of the electromagnetic flux leaving the system and the rate of work done on the static

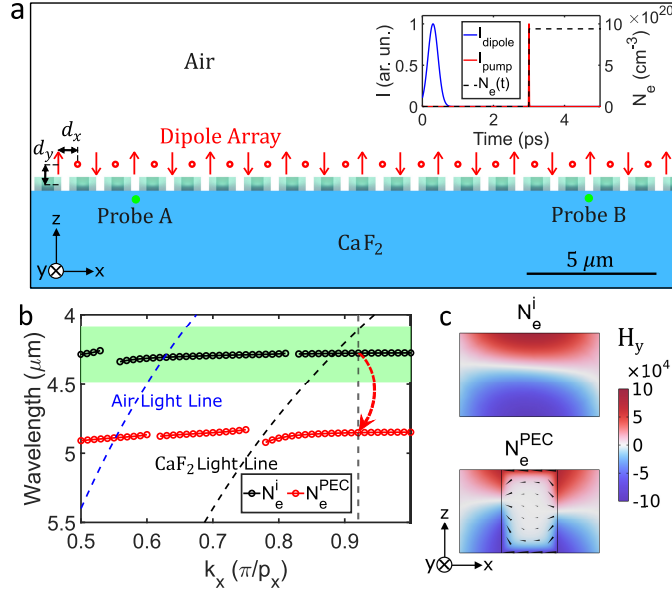


Figure 3: **a.** Setup used for TI simulations where the shaded red region shows the cylindrical hot spots of radius 200 nm inside each meta-atom. Probe points are located in the substrate (green circles). MGW is launched using a dipole array (red arrows) separated by  $d_x = \pi/2k_x$  and at a height  $d_y = \lambda_0/4$  above the metasurface; the length of the arrows represents the magnitude of the dipole moment. Inset: Pump pulse (red) and dipolar excitation (blue) intensity and the temporal variation of hot spot FC density (black dashed). **b.** Dispersion plot of the ED mode for hot spot FC density,  $N_e^i = 0 \text{ cm}^{-3}$  (black circles) and  $N_e^{\text{PEC}} = 9.4 \times 10^{20} \text{ cm}^{-3}$  (red circles); the green shaded region indicates the spectrum of the dipolar excitation. Red dashed arrow: redshifting of the ED mode when the hot spot FC density is increased from  $N_e^i$  to  $N_e^{\text{PEC}}$ . **c.**  $H_y$  field profile of the ED mode (in the x-z midplane) before (top) and after (bottom) the TI; the black cones indicate the FC current density in the hot spot.

currents created in the system during a TI. We emphasize that  $\mathbf{J}_{e,s}$  is a constant current density related to the DC motion of the FCs that is created during a TI and persists even after the departure of the electromagnetic waves. Integrating eq. 15, followed by algebraic simplification and integration by parts (see Section V of the SI for detailed derivations), yields

$$\begin{aligned} U = & \frac{1}{2}\epsilon_0|\mathbf{E}|^2 + \frac{1}{2}\mu_0|\mathbf{H}|^2 + \frac{1}{2}\epsilon_0(\epsilon_\infty - 1)|\mathbf{E}|^2 + \frac{1}{2}\epsilon_0\omega_p^2|\mathbf{A}|^2 \\ & + \int_{-\infty}^t \frac{\partial N_e^{(2)}}{\partial t'} \frac{|e\mathbf{A}(t')|^2}{2m_e} dt' - \mathbf{A}(t) \cdot \left( \frac{e^2}{m_e} \int_{-\infty}^t \frac{\partial N_e^{(2)}}{\partial t'} \mathbf{A}(t') dt' \right) \end{aligned} \quad (18)$$

The expression above for the total energy density holds at all times, including the time before, within, and after the time interface. The first (second) term on the RHS of eq.(18) represents the energy density stored in the form of electric (magnetic) fields, while the third term represents the potential energy density stored in the bound electrons. The sum of the first three terms is labeled  $U_1 = \frac{1}{2}\epsilon_0\epsilon_\infty|\mathbf{E}|^2 + \frac{1}{2}\mu_0|\mathbf{H}|^2$ , while the sum of the remaining terms represents the energy density stored in the FCs and is labeled  $U_2 = \frac{1}{2}\epsilon_0\omega_p^2|\mathbf{A}|^2 + \int_{-\infty}^t \frac{\partial N_e^{(2)}}{\partial t'} \frac{|e\mathbf{A}(t')|^2}{2m_e} dt' - \mathbf{A}(t) \cdot \left( \frac{e^2}{m_e} \int_{-\infty}^t \frac{\partial N_e^{(2)}}{\partial t'} \mathbf{A}(t') dt' \right)$ . In the next section, we use eq. (18) to calculate and compare the total energies for the cases with a TI and without a TI.

## 4 Impact of a Time Interface in a metasurface

### 4.1 Time reflection and refraction of a MGW at TI

The TI is created by FCG in the hot spot under an intense pump pulse illumination, resulting in a time-varying metasurface. A wave propagating along the metasurface senses this TI and is temporally scattered. We modify the dimensions of the metasurface to obtain an ED MGW near the edge of the Brillouin zone ( $w_x \times w_y \times w_z : 1 \text{ } \mu\text{m} \times 1.7 \text{ } \mu\text{m} \times 0.6 \text{ } \mu\text{m}$  and  $p_x \times p_y : 1.35 \text{ } \mu\text{m} \times 2 \text{ } \mu\text{m}$ ). We will

use this metasurface design in the subsequent sections. Metasurface eigenmode and TI simulations are performed using COMSOL Multiphysics. The metasurface dispersion plot for the ED mode is shown in Fig. 3b for the unperturbed (black line) and perturbed (red line) cases. Although the ED mode of the metasurface leaks into the  $\text{CaF}_2$  substrate for most of the Brillouin zone, it drops below the light line and becomes an ED MGW (decaying in the  $z$  direction away from the metasurface) near the edge of the Brillouin zone ( $|k_x| \gtrsim 0.89 \cdot \pi/p_x$ ). We excite an ED MGW, propagating in the  $x$  direction with  $k_x = 0.92\pi/p_x$ ,  $k_y = k_z = 0$  (dashed gray line in Fig. 3b)  $\varepsilon_{hs} = \varepsilon_{ini}$ . The MGW has a larger wave vector than the free-space light at  $|k_x| = 0.92\pi/p_x > 2\pi/\lambda_0$ , where  $\lambda_0 = 4.27 \mu\text{m}$  is the central wavelength of dipolar excitation, which corresponds to the ED mode of the modified metasurface. Thus, we used an array of phased electric dipoles to excite the MGW. These dipoles are shown as red arrows in Fig. 3a with spacing  $d_x = \pi/2k_x$  located at a height  $d_y = \lambda_0/4$  above the metasurface with dipole moments pointing in the  $\hat{z}$  direction. The dipole moment at the location of the  $n$ -th dipole  $x_n = nd_x$  ( $n=1,2,3,\dots$ ) and at time  $t$  is given by  $\mathbf{p}_{\text{dipole}}(x_n, t) = \mathbf{p}_0 \cos(k_x x_n - \omega_0 t) e^{-(t-\tau_2)^2/\tau_0^2} \hat{z}$  (where  $\omega_0 = 2\pi c/\lambda_0$ ,  $\mathbf{p}_0 = 1 \text{ C-m}$   $\tau_2 = 300 \text{ fs}$  and  $\tau_0 = 200 \text{ fs}$ ). The green shaded region in Fig. 3b shows the spectrum of dipolar excitation. This phased dipole array is essential to efficiently excite the MGW at a specific  $k_x$ , as the dispersion line for the ED MGW is extremely flat.

Alterations in the constitutive materials of the metasurface over time (e.g., controlled LFCG at the hot spot) modify the metasurface, resulting in a time-varying medium for the MGW. For the pump pulse parameters given in Section 3.1, we calculated the FC concentration in the hot spot using eq. (6) and the transition time in which  $N_e$  changes from  $N_e^i$  to  $N_e^{\text{PEC}}$  is  $T_{\text{trans}} \approx 10 \text{ fs} < T_0 = 2\pi/\omega_0 \approx 14.27 \text{ fs}$ . The transition from  $N_e^i$  to  $N_e^{\text{PEC}}$  occurs in less than an optical cycle of the MGW, thus creating a sharp TI for the propagating MGW. The simulation setup used to implement a TI during MGW propagation is shown in Fig. 3a, where the cylindrical red volume in each meta-atom denotes the hot spot region where the FC density can be varied by the intensity of the pump pulse. The probe points where we inspect the signal are marked as yellow circles in Fig. 3a. We compare the  $H_y$  field profiles at 4955 fs in the cases with and without a TI. For the case without a TI, the MGW crosses approximately 8 meta-atom unit cells (dashed black box in the left field plot in Fig. 4a) from left to right in the simulation domain, propagating at a group velocity of  $v_g^i \approx 0.007c$ , where  $c$  is the speed of light in vacuum. We compare this case against the case with a TI at 3000 fs. In 3000 fs, the MGW propagates across 5 meta-atoms. However, at 4955 fs in the case with a TI, we observe that the MGW has backpropagated, crossing approximately 4 meta-atoms propagating at a group velocity of  $v_g^{\text{PEC}} \approx 0.009c$  (dashed black box in the right field plot in Fig. 4a). This indicates the presence of a time-reflected MGW signal. Although the time-reflected signal in the negative  $x$  direction is a signal of temporal scattering of a MGW from the sharp TI, stronger evidence can be found by inspecting the spectrum of light[56]. The  $x$  component of the electric field ( $E_x$ ) is recorded at the two probe locations. Fourier transforms of  $E_x$  for the two cases, with a TI at 3000 fs ( $|\text{FT}(E_{\text{PEC}})|^2$ ) and without a TI ( $|\text{FT}(E_i)|^2$ ), are shown in Fig. 4b. In both cases, we focus exclusively on the electric field measured after 3000 fs. For the case without a TI, we observed a peak in the spectrum (black dashed and bold lines in Fig. 4b) at 70.1 THz corresponding to the ED resonance of the metasurface at both probe points (weaker signal at probe A). Now, in the presence of a sharp TI (red dashed and bold lines in Fig. 4b), the spectrum of the field recorded at both probe points exhibits a clearly red-shifted ED peak at 61.68 THz (stronger signal of time-reflected, red-shifted MGW at probe A). Thus, we see that the TI due to  $N_e$  changing from  $N_e^i \rightarrow N_e^{\text{PEC}}$  results in the redshifting of the MGW by exactly the amount predicted by the mode dispersions for  $N_e^i$  and  $N_e^{\text{PEC}}$  FC densities.

## 4.2 Energy Dynamics Across a Time Interface

We consider pre-existing FC density  $N_e^{(1)} = 0$  for the TI simulations. We integrate the expressions for the energy densities from eq. (18) over the simulation domain to calculate the time evolution of the energy contributions of the different terms (that is,  $E_1 = \int U_1 dV$ , and  $E_2 = \int U_2 dV$ ). We calculate the difference in  $E_1$ ,  $E_2$ , and also the total energy of the system ( $E_{\text{Total}} = \int U dV$ ) for the cases with and without TI ( $\Delta E_{\text{Total}} = \Delta E_1 + \Delta E_2$ ;  $\Delta E = E(\text{TI}) - E(\text{No TI})$ ). In Fig. 4c, we observe that when TI is introduced,  $\Delta E_1$  decreases, while  $\Delta E_2$  increases by an equal magnitude. Note that  $\Delta E_{\text{Total}}$  drops slightly below the zero line after the TI. This can be ascribed to the fact that the group velocity and the quality factor of the MGW change after TI. In any case, ignoring these small contributions to the total energy, our simulations indicate that the total energy of the system in the case of TI remains the same as that in the case of no TI, when the FCs are generated at rest. Analytically, it is written as  $U(\text{no TI})|_{t>t_{\text{TI}}} = U(\text{TI})|_{t>t_{\text{TI}}}$ , where we evaluate the energy densities for the two cases at a time after the time interface ( $t > t_{\text{TI}}$ ). Now, for the case of no TI, we use the unperturbed fields ( $\mathbf{E}_0$ ,  $\mathbf{H}_0$ ,  $\omega_0$ ) to calculate the energy

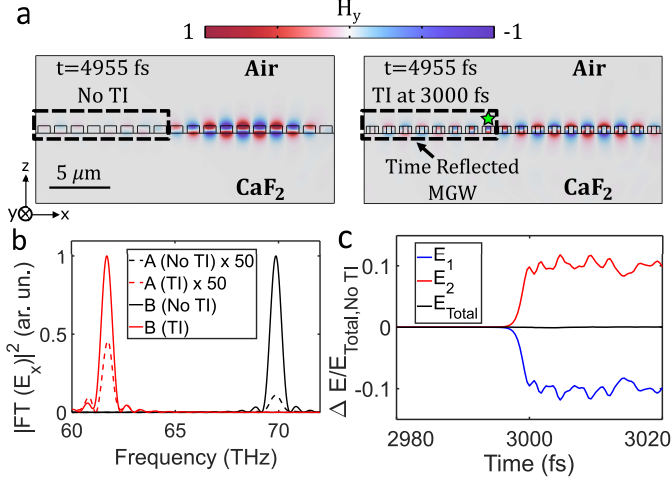


Figure 4: **a.** Normalized  $H_y$  profile in the x-z mid-plane of the simulation domain on the left (right) shows the MGW propagating with group velocity  $v_g^i \approx 0.007c$  ( $v_g^{\text{PEC}} \approx 0.009c$ ) without a TI (with a TI) at  $t=4955$  fs; the rectangular region inside each meta-atom represents the cylindrical hot spot of radius 200 nm. **b.**  $|\text{FT}(E_x)|^2$  recorded at the two probe locations after the TI for the two cases: without a TI where  $N_e^{(2)} = N_e^i = 0 \text{ cm}^{-3}$  throughout (black dashed (bold) line at Probe A (B)), and with a TI where  $N_e^{(2)} = N_e^{\text{PEC}} = 9.4 \times 10^{20} \text{ cm}^{-3}$  after the TI (red dashed (bold) line at Probe A (B)). **c.** Time evolution of the contributions ( $E_1$ : blue line,  $E_2$ : red line) to the total energy ( $E_{\text{Total}}$ : black line).

density  $U(\text{no TI})|_{t>t_{\text{TI}}}$  after the TI, which, time averaged over an optical cycle, can be written as

$$U(\text{no TI})|_{t>t_{\text{TI}}} = U_{\text{EM}}(\text{no TI}) = \frac{1}{2}\epsilon_0\epsilon_{\infty}\langle|\mathbf{E}_0|^2\rangle + \frac{1}{2}\mu_0\langle|\mathbf{H}_0|^2\rangle + \frac{1}{2}\epsilon_0\left(\frac{\omega_{p0}^2}{\omega_0^2}\right)\langle|\mathbf{E}_0|^2\rangle \quad (19)$$

where  $\omega_{p0}$  and  $U_{\text{EM}}$  (no TI) are the plasma frequency and the electromagnetic energy density for the case without TI, respectively. Here, ' $\langle \rangle$ ' denotes the time-averaged quantity over an optical cycle of the wave's frequency. However, for the case of TI, to calculate the time-averaged total energy density, we use eq. (13) in eq. (18) to separate the energy density in propagating electromagnetic fields from the energy density in the QS mode such that  $U(\text{TI})|_{t>t_{\text{TI}}} = U_{\text{EM}}(\text{TI}) + U_{\text{QS}}$ .

$$U_{\text{EM}}(\text{TI}) = \frac{1}{2}\epsilon_0\epsilon_{\infty}\langle|\mathbf{E}_t|^2\rangle + \frac{1}{2}\mu_0\langle|\mathbf{H}_t|^2\rangle + \frac{1}{2}\epsilon_0\left(\frac{\omega_p^2}{\omega_f^2}\right)\langle|\mathbf{E}_t|^2\rangle \quad (20)$$

Here,  $U_{\text{EM}}(\text{TI})$  is the electromagnetic energy density for the case of TI. The energy density in the hot spot due to the QS mode of the system can be expressed using the quasistatic magnetic field ( $\mathbf{H}_s$ ) and the quasistatic magnetic vector potential ( $\mathbf{A}_s$ ) derived in eq. (14) as

$$U_{\text{QS}} = \frac{1}{2}\mu_0|\mathbf{H}_s|^2 + \frac{1}{2}\epsilon_0\omega_p^2|\mathbf{A}_s|^2 + \int_{-\infty}^t \frac{\partial N_e^{(2)}}{\partial t'} \frac{|e\mathbf{A}(t')|^2}{2m_e} dt' - \mathbf{A}_s \cdot \left( \frac{e^2}{m_e} \int_{-\infty}^t \frac{\partial N_e^{(2)}}{\partial t'} \mathbf{A}(t') dt' \right) \quad (21)$$

From eqs. (19,20,21), it follows that in the case of TI, the electromagnetic energy is depleted by the same amount as the energy expended to create DC currents, which analytically is written as  $U_{\text{EM}}(\text{TI}) - U_{\text{EM}}(\text{no TI}) = \Delta U_{\text{EM}} = -U_{\text{QS}}$ . Numerically, we find  $U_{\text{QS}} > 0$ , which implies that the electromagnetic energy density in the MGW decreases, while the energy density in the QS mode increases across the TI.

### 4.3 Nanoscale Magnetization Using Rapid FC Generation

The electrons generated at rest inside the hot spot during the TI are accelerated by the electric field and, once they have non-zero velocity, the magnetic field of the mid-IR MGW present in the hot spot region.

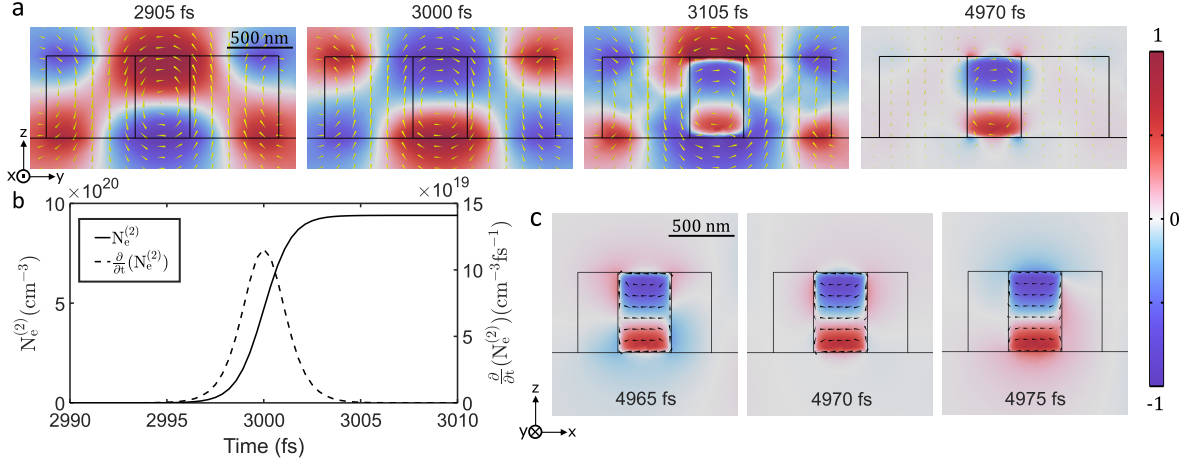


Figure 5: **a.** Normalized  $H_y$  profile in the  $y$ - $z$  mid-plane of the meta-atom marked using a light green star in Fig. 4a, at 2905 fs, 3000 fs, and 3105 fs; the yellow cones represent the magnetic field lines **b.** Time evolution of FC density and its temporal derivative. **c.** Time evolution of the QS mode at three consecutive time steps separated by  $\Delta t = 5$  fs in the  $x$ - $z$  midplane of the same meta-atom; the black cones indicate the FC current density in the hot spot. The rectangular region inside the meta-atom in all plots represents the cylindrical hot spot of radius 200 nm. The light green star shows the meta-atom where we show the magnetic field in Fig. 5.

After the TI, the large number of FCs in the hot spot screen the MGW electric field. Consequently, the displacement currents in the hot spot volume before the TI due to the AC electric field of the MGW are replaced by real electric currents because of the motion of the FCs in the hot spot after the TI. These circulating currents inside the hot spot result in a quasistatic magnetic field that is obtained by rectifying the AC magnetic field of the MGW during the TI. The acceleration of the FCs that are created during the TI by the mid-IR MGW is driven by the magnetic vector potential,  $\mathbf{A}(t)$ , of the MGW as shown in eq. (9). The long wavelength mid-IR MGW is better able to accelerate the electrons because  $\mathbf{A}(t)$  scales linearly with the wavelength. Additionally, the energy of the longer wavelength photon in the mid-IR MGW is smaller than the Ge bandgap, which eliminates the probability of single-photon absorption and consequently the possibility of FC generation. Another process that can cause FC generation by the mid-IR MGW is multiphoton absorption. However, the multiphoton absorption probability of a mid-IR MGW is drastically reduced because the Keldysh parameter for the MGW, which is approximately the ratio of the TI duration to the MGW optical cycle, is less than one[57]. The rectification of the magnetic field of an electromagnetic wave upon the rapid creation of a plasma around a portion of the wave was studied several decades ago [31]. More recently, the rectification of electric fields in capacitive metasurfaces due to a time interface has been reported [16]. The opposite effect has also been predicted, where a static electric field is partially converted to a dynamic radiation field at a time interface [58]. Here, we demonstrate the rectification of the resonantly enhanced magnetic field of a MGW that is dependent on the full-vector, three-dimensional optical fields of the MGW in the hot spot.

#### 4.3.1 Quasistatic Magnetic Field

The rectification of the magnetic field of the MGW at the TI is shown in Fig. 5a, which shows snapshots of  $H_y$  in the  $y$ - $z$  mid-plane at different times inside the meta-atom and its vicinity in air and the substrate. The yellow cones show the direction of the magnetic field.  $H_y$  is normalized to the peak field of steady-state MGW before TI. The first panel of Fig. 5a shows the magnetic field at 2905 fs,  $\sim 6.5$  optical cycles before the TI, when there are no FCs in the hot spot ( $N_e^{(2)} = 0$ ). The second (third) panel shows the magnetic field of the MGW at 3000 (3105) fs, during (after) the TI. Compared to the snapshots before and during the TI, the third panel, which shows the snapshot  $\sim 6.5$  optical cycles after the TI, shows drastic differences in the spatial structure magnetic field. Although the field outside the hot spot region at 3105 fs has a spatial structure similar to that at 2905 fs, the magnetic field in the hot spot region (smaller rectangle in the center of each panel) retains the spatial pattern of the magnetic field in that region at 3000 fs. This is the rectified quasistatic magnetic field that results from the TI and corresponds to the QS mode. The fourth panel in Fig. 5a shows the magnetic field after  $\sim 121.5$

optical cycles after the TI at 4970 fs. We find that, in the absence of losses, the QS mode persists even as the fields outside the hot spot become weaker because the time-refracted MGW has moved past, and only the weaker, time-reflected MGW remains in the region shown.

The spatial structure of the rectified magnetic field that persists in the hot spot resembles that of the MGW magnetic field in the hot spot region at 3000 fs. This phenomenon can be understood from eq. (14), which shows that the source term for the quasistatic magnetic vector potential  $\mathbf{A}_s$  is a weighted integral of the magnetic vector potential of the MGW during TI where the weights are  $\partial N_e^{(2)}/\partial t$ . Thus, the largest contribution to the rectified magnetic field is from the instant during the TI where the  $\partial N_e^{(2)}/\partial t$  is maximum, which in our case is 3000 fs (where the MGW optical fields are almost at their peak), as shown in Fig. 5b. The rectification of the magnetic field is not perfectly efficient even when we ignore the effect of losses. The peak value of the rectified magnetic field is  $\sim 82\%$  of the peak value of the AC magnetic field of the MGW. This may be attributed to two factors: (i) the finite duration of the time interface, which is  $\sim 13$  fs in the case shown in Fig. 5, and (ii) even a slight mismatch between the peak of  $\partial N_e^{(2)}/\partial t$ , with the peak of the MGW optical fields during the optical cycle. An instantaneous TI at a time instant when the MGW optical fields are at their peak could allow perfectly efficient rectification, but that is an unphysical scenario [31]. Further, it must be noted that a very long TI that stretches over many optical cycles of the MGW would lead to the rectification averaging over many optical cycles, resulting in a near-zero amplitude.

Further evidence of the static nature of the QS mode can be seen in Fig. 5c from the  $x - z$  midplane snapshots that show the field  $H_y$  in three time steps separated by  $\Delta t = 5$  fs =  $0.31 T_f$  (where  $T_f = 16.21$  fs is the optical cycle of the frequency-shifted MGW). Even as the fields outside the hot spot change with time because of the propagation of the time-reflected MGW at different points in the optical cycle, the QS mode remains unchanged. The electric currents in the hot spot (black cones in the smaller rectangle in the center), which replace the displacement currents during the TI and maintain the quasistatic magnetic field, remain mostly unchanged across the optical cycle of the frequency-shifted MGW, though there are small alterations near the boundary of the hot spot where the electrons screen the electric field of the time-reflected MGW outside the hot spot.

The absolute magnitude of the rectified magnetic field in the QS mode,  $\mathbf{H}_s$ , depends on the optical fields of the MGW. The maximum optical field of MGW that may propagate along the metasurface is, in turn, limited by the laser-induced damage threshold of Ge, which has been measured as  $1.7$  TW/cm $^2$  at  $3.6$   $\mu$ m [59]. We obtain a peak magnetic field amplitude of  $\sim 8.8$  T when we excite the MGW such that the resonantly enhanced MGW intensity does not exceed  $1$  TW/cm $^2$  anywhere in the Ge meta-atom. With  $\sim 82\%$  rectification of the MGW magnetic field for the TI being considered, the peak rectified magnetic field amplitude is  $\sim 7.2$  T. Thus, we find that rectification of a resonantly enhanced AC magnetic field due to a TI via LFCG offers a new paradigm to realize giant, nanoscale magnetization without the use of any external magnetic field.

#### 4.3.2 Effects of Losses

In the absence of losses, the rectified magnetic field persists, and its magnitude remains nearly constant. However, the persistence of the QS mode is hindered by the disruption of quasistatic currents due to the scattering of electrons by other electrons, ions, and phonons. We consider an arbitrary electronic scattering frequency  $\gamma_{\text{scattering}} = 4.73 \times 10^{13}$  rad/s, which encapsulates the contributions due to various scattering mechanisms. This leads to a modification of eq. (11) where a damping term is introduced as

$$\frac{\partial^2 \mathbf{P}_e}{\partial t^2} + \gamma_{\text{scattering}} \frac{\partial \mathbf{P}_e}{\partial t} = \epsilon_0 \omega_p^2(t) \mathbf{E} \quad (22)$$

Due to these losses, the electronic currents supporting the quasistatic magnetic field eventually decay, and the zero magnetic field region near the center of the hot spot diffuses until it occupies the entire hot spot. This process is known as magnetic diffusion and, in our case, follows the magnetic diffusion equation[60]

$$\frac{\partial \mathbf{H}}{\partial t} = \frac{1}{\mu_0 \sigma_0} \nabla^2 \mathbf{H} = D \nabla^2 \mathbf{H} \quad (23)$$

where the electronic diffusion constant  $D = 1/\mu_0 \sigma_0$  and  $\sigma_0$  is the electrical DC conductivity, which is inversely proportional to  $\gamma_{\text{scattering}}$ . Furthermore, to quantify the persistence of the QS mode after the TI, we focus on the rectified quasistatic magnetic field and consider the difference between its peak positive and peak negative magnetic fields. We do this by considering two regions in the  $x$ - $z$  midplane inside the hot spot where the QS mode is dominant over the MGW as shown in Fig. 6b and calculate

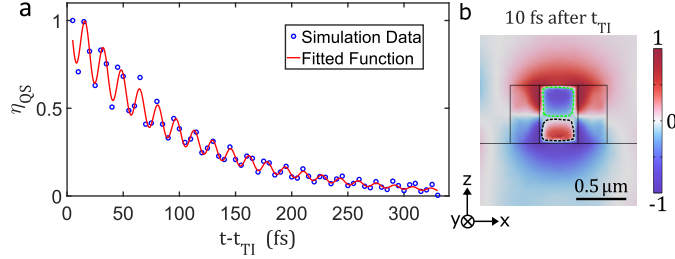


Figure 6: **a.**  $\eta_{QS}$  after the time interface, the open circles show the simulation data, while the red line shows the bi-exponential decay function shown in eq. (25) fitted to the simulation data. **b.** The rectified magnetic field 10 fs after the TI. The dashed polygons enclose the regions inside the hot spot used to calculate  $\Delta H_{QS}(t)$ .

$\Delta H_{QS}$  by subtracting the minimum magnetic field amplitude in the region enclosed by the dotted green line from the maximum magnetic field amplitude in the region enclosed by the dotted black line. Then, we define a normalized quantity  $\eta_{QS}$ , which is calculated as

$$\eta_{QS}(t) = \frac{\Delta H_{QS}(t)}{\max.(\Delta H_{QS}(t))}. \quad (24)$$

Thus, lower values of  $\eta_{QS}$  correspond to smaller amplitudes of the QS mode at the hot spot. We fit the simulation data for  $\eta_{QS}$  using a bi-exponential decay function that accounts for the decay of the temporally scattered MGW as well as the diffusion of  $\mathbf{H}_s$  in the presence of losses

$$\eta_{QS} = Ae^{-i\omega_f t} + Be^{-\gamma_{\text{diff}} t}; \omega_f = \omega_{fr} - i\gamma_f, \quad (25)$$

where  $\omega_{fr} = 3.88 \times 10^{14}$  rad/s, is the angular frequency of the red-shifted MGW as shown in Fig. 4b. In Fig. 6a, which shows the temporal evolution of  $\eta_{QS}$ , the open circles represent the simulation data points, while the red line represents the function shown in eq. (25) fitted to the simulation data and plotted over a denser time grid. From the fitted function, we obtain  $A = 0.173$ ,  $B = 0.997$ ,  $\gamma_f = 1.3 \times 10^{12}$  rad/s, and  $\gamma_{\text{diff}} = 1.013 \times 10^{13}$  rad/s. The ratio  $B/A \approx 5.75$  indicates that the rectified quasistatic magnetic field dominates over the AC magnetic field due to the MGW in areas selected for calculating  $\eta_{QS}$ . Furthermore, the diffusion time of the static currents inside the hot spot,  $T_{\text{diff}} = 1/\gamma_{\text{diff}} = 98.68$  fs. Thus,  $T_{\text{diff}} \approx 5 \gamma_{\text{scattering}}^{-1}$  and we find that even in the presence of electron scattering losses, the QS mode persists over a time scale substantially longer than a single scattering time.

## 5 Conclusion

In conclusion, we have presented a method for the tunable shifting of a high- $Q$  resonance in an all-dielectric metasurface that is resonant in the mid-IR via controlled LFCG in a cylindrical hot spot region within the meta-atoms. We derived an analytic expression for the frequency shift, taking into account the full vectorial form of the unperturbed electromagnetic fields integrated over the perturbed volume along with the perturbation to the permittivity, that accurately predicts the blueshift of the metasurface resonance due to FCG in the hot spot in the perturbative regime. We found that for low FC densities in the hot spot, the resonance blueshifts. However, a further increase in FC density that effectively metalizes the hot spot ( $\epsilon_{hs} \ll 0$ ) results in a strongly red-shifted resonance frequency. Thus, in an experimental setting, carefully tuning the pump intensity to control the local FC density at the hot spot would allow tunable blue- or redshifting of the metasurface resonance.

We have further demonstrated that the shift in the metasurface resonance via LFCG has the potential to serve as a platform for the study of time-varying photonics at mid-IR frequencies. We studied the effect of LFCG in an array of hot spots at the center of each meta-atom, where we calculated the FC generation due to a pump pulse using the Keldysh model. Modeling each hot spot as a time-dependent Drude-Lorentz medium with a rapidly changing plasma density, we described a theoretical framework for incorporating the effects of rapid free carrier generation over short but finite time scales into time-domain electromagnetic codes. Implementing a sharp TI using LFCG for a mid-IR MGW, we observed temporal reflections, including a redshift of the time-reflected waves. Furthermore, using Poynting's Theorem, we identified various contributions to the total energy and derived an analytic expression for the total

energy density in a time-varying Drude-Lorentz medium. We demonstrated the re-partitioning of the incident MGW energy into time-reflected/refracted MGW and persistent electric currents and magnetic fields in the domain where LFCG occurs. By comparing the cases with and without a TI, we validated that the total energy in a time-varying system remains unaffected by the FCs created at rest during a TI. Additionally, after TI, a large, highly localized, and persistent quasistatic magnetic field (QS mode) is observed in the hot spot that does not radiate but consumes a substantial part of the electromagnetic energy. Using the TI created from LFCG, we provided evidence of efficient rectification ( $\sim 82\%$ ) of the resonantly enhanced AC magnetic field due to the MGW in the hot spot. This shows that a time interface realized via rapid FC generation in an all-dielectric metasurface can serve as a novel platform that allows efficient conversion of an AC optical field at  $\omega$  frequency to a DC optical field even in the absence of strong nonlinear properties of the constituent materials. These results significantly enhance and clarify our understanding of the energy dynamics in a time-varying medium and the rectification of magnetic fields at a TI. We are optimistic that our findings will open new directions of research in optically tunable metasurfaces as a platform for time-varying photonics.

## Disclosures

The authors declare no competing interests.

## Code and Data

The data that support the findings of this study are available from the corresponding authors upon request.

## Acknowledgments

The authors would like to thank Yandong Li for fruitful discussions regarding resonance frequency shifting in cavities. The work at Cornell was supported by the University of Dayton Research Institute (UDRI) under the contract FA8651-24-F-B013, Office of Naval Research (ONR) under the grant no. N00014-21-1-2056, and the Army Research Office (ARO) under the award W911NF2110180.

## References

- [1] E. Yablonovitch, “Self-phase modulation of light in a laser-breakdown plasma,” *Physical Review Letters*, vol. 32, pp. 1101–1104, May 1974.
- [2] S. C. Wilks, J. M. Dawson, W. B. Mori, T. Katsouleas, and M. E. Jones, “Photon accelerator,” *Physical Review Letters*, vol. 62, pp. 2600–2603, May 1989.
- [3] E. Yablonovitch, “Spectral broadening in the light transmitted through a rapidly growing plasma,” *Physical Review Letters*, vol. 31, pp. 877–879, Oct 1973.
- [4] W. M. Wood, C. W. Siders, and M. C. Downer, “Measurement of femtosecond ionization dynamics of atmospheric density gases by spectral blueshifting,” *Physical Review Letters*, vol. 67, pp. 3523–3526, Dec 1991.
- [5] R. L. Savage, C. Joshi, and W. B. Mori, “Frequency upconversion of electromagnetic radiation upon transmission into an ionization front,” *Physical Review Letters*, vol. 68, pp. 946–949, Feb 1992.
- [6] M. Shcherbakov, K. Werner, Z. Fan, N. Talisa, E. Chowdhury, and G. Shvets, “Photon acceleration and tunable broadband harmonics generation in nonlinear time-dependent metasurfaces,” *Nature Communications*, vol. 10, 03 2019.
- [7] C. Liu, M. Z. Alam, K. Pang, K. Manukyan, O. Reshef, Y. Zhou, S. Choudhary, J. Patrow, A. Pen-nathurs, H. Song, Z. Zhao, R. Zhang, F. Alishahi, A. Fallahpour, Y. Cao, A. Almaiman, J. M. Dawlaty, M. Tur, R. W. Boyd, and A. E. Willner, “Photon acceleration using a time-varying epsilon-near-zero metasurface,” *ACS Photonics*, vol. 8, no. 3, 2021.

[8] K. Pang, M. Z. Alam, Y. Zhou, C. Liu, O. Reshef, K. Manukyan, M. Voegtle, A. Pennathur, C. Tseng, X. Su, H. Song, Z. Zhao, R. Zhang, H. Song, N. Hu, A. Alaiman, J. M. Dawlaty, R. W. Boyd, M. Tur, and A. E. Willner, “Adiabatic frequency conversion using a time-varying epsilon-near-zero metasurface,” *Nano Letters*, vol. 21, no. 14, pp. 5907–5913, 2021.

[9] J. Mendonca, *Theory of Photon Acceleration*. Series in Plasma Physics, Boca Raton: CRC Press, 2000.

[10] X. Wang, M. S. Mirmoosa, V. S. Asadchy, C. Rockstuhl, S. Fan, and S. A. Tretyakov, “Metasurface-based realization of photonic time crystals,” *Science Advances*, vol. 9, no. 14, p. eadg7541, 2023.

[11] X. Wang, P. Garg, M. S. Mirmoosa, A. Lamprianidis, C. Rockstuhl, and V. Asadchy, “Expanding momentum bandgaps in photonic time crystals through resonances,” *Nature Photonics*, pp. 1–7, 11 2024.

[12] M. R. Shcherbakov, R. Lemasters, Z. Fan, J. Song, T. Lian, H. Harutyunyan, and G. Shvets, “Time-variant metasurfaces enable tunable spectral bands of negative extinction,” *Optica*, vol. 6, pp. 1441–1442, Nov 2019.

[13] V. Pacheco-Pena and N. Engheta, “Antireflection temporal coatings,” *Optica*, vol. 7, pp. 323–331, Apr 2020.

[14] A. R. Katko, S. Gu, J. P. Barrett, B.-I. Popa, G. Shvets, and S. A. Cummer, “Phase conjugation and negative refraction using nonlinear active metamaterials,” *Physical Review Letters*, vol. 105, p. 123905, Sep 2010.

[15] A. Akbarzadeh, N. Chamanara, and C. Caloz, “Inverse prism based on temporal discontinuity and spatial dispersion,” *Optics Letters*, vol. 43, pp. 3297–3300, Jul 2018.

[16] X. Wang, M. S. Mirmoosa, and S. A. Tretyakov, “Controlling surface waves with temporal discontinuities of metasurfaces,” *Nanophotonics*, vol. 12, no. 14, pp. 2813–2822, 2023.

[17] L. Stefanini, S. Yin, D. Ramaccia, A. Alù, A. Toscano, and F. Bilotti, “Temporal interfaces by instantaneously varying boundary conditions,” *Physical Review B*, vol. 106, p. 094312, Sep 2022.

[18] E. Galiffi, Y.-T. Wang, Z. Lim, J. B. Pendry, A. Alù, and P. A. Huidobro, “Wood anomalies and surface-wave excitation with a time grating,” *Physical Review Letters*, vol. 125, p. 127403, Sep 2020.

[19] R. Tirole, S. Vezzoli, E. Galiffi, I. Robertson, D. Maurice, B. Tilmann, S. A. Maier, J. B. Pendry, and R. Sapienza, “Double-slit time diffraction at optical frequencies,” *Nature Physics*, vol. 19, p. 999–1002, Apr. 2023.

[20] H. Moussa, G. Xu, S. Yin, E. Galiffi, Y. Radi, and A. Alu, “Observation of temporal reflection and broadband frequency translation at photonic time interfaces,” *Nature Physics*, pp. 1–6, 2022.

[21] E. Galiffi, G. Xu, S. Yin, H. Moussa, Y. Radi, and A. Alù, “Broadband coherent wave control through photonic collisions at time interfaces,” *Nature Physics*, vol. 19, 12 2022.

[22] E. Galiffi, R. Tirole, S. Yin, H. Li, S. Vezzoli, P. A. Huidobro, M. G. Silveirinha, R. Sapienza, A. Alu, and J. B. Pendry, “Photonics of time-varying media,” *Advanced Photonics*, vol. 4, no. 1, p. 014002, 2022.

[23] M. Z. Alam, I. D. Leon, and R. W. Boyd, “Large optical nonlinearity of indium tin oxide in its epsilon-near-zero region,” *Science*, vol. 352, no. 6287, pp. 795–797, 2016.

[24] M. Z. Alam, S. A. Schulz, S. A. Schulz, S. A. Schulz, J. Upham, I. D. Leon, R. W. Boyd, and R. W. Boyd, “Large optical nonlinearity of nanoantennas coupled to an epsilon-near-zero material,” *Nature Photonics*, vol. 12, pp. 79–83, 2018.

[25] Y. Yang, J. Lu, A. Manjavacas, T. S. Luk, H. Liu, K. P. Kelley, J. Maria, E. L. Runnerstrom, M. B. Sinclair, S. Ghimire, and I. Brener, “High-harmonic generation from an epsilon-near-zero material,” *Nature Physics*, pp. 1–5, 2019.

[26] M. Clerici, N. Kinsey, C. DeVault, J. Kim, E. Carnemolla, L. Caspani, A. Shaltout, D. Faccio, V. Shalaev, A. Boltasseva, and M. Ferrera, “Controlling hybrid nonlinearities in transparent conducting oxides via two-colour excitation,” *Nature Communications*, vol. 8, 06 2017.

[27] L. V. Keldysh, “Ionization in the field of a strong electromagnetic wave,” *Journal of Experimental and Theoretical Physics*, vol. 20, no. 5, pp. 1307–1314, 1965.

[28] V. E. Gruzdev, “Fundamental mechanisms of laser damage of dielectric crystals by ultrashort pulse: ionization dynamics for the keldysh model,” *Optical Engineering*, vol. 53, no. 12, p. 122515, 2014.

[29] C. Bosshard, R. Spreiter, M. Zgonik, and P. Gunter, “Kerr nonlinearity via cascaded optical rectification and the linear electro-optic effect,” *Physical Review Letters*, vol. 74, pp. 2816–2819, Apr 1995.

[30] J. A. Fülöp, S. Tzortzakis, and T. Kampfrath, “Laser-driven strong-field terahertz sources,” *Advanced Optical Materials*, vol. 8, no. 3, p. 1900681, 2020.

[31] S. C. Wilks, J. M. Dawson, and W. B. Mori, “Frequency up-conversion of electromagnetic radiation with use of an overdense plasma,” *Physical Review Letters*, vol. 61, pp. 337–340, Jul 1988.

[32] A. Fernandez-Pacheco, R. Streubel, O. Fruchart, R. Hertel, P. Fischer, and R. P. Cowburn, “Three-dimensional nanomagnetism,” *Nature Communications*, vol. 8, no. 1, p. 15756, 2017.

[33] V. Levati, M. Vitali, A. Del Giacco, N. Pellizzi, R. Silvani, L. Ciaccarini Mavilla, M. Madami, I. Biancardi, D. Girardi, M. Panzeri, *et al.*, “Three-dimensional nanoscale control of magnetism in crystalline yttrium iron garnet,” *Nature Communications*, vol. 16, no. 1, p. 9602, 2025.

[34] K. Hao, R. Shreiner, A. Kindseth, and A. A. High, “Optically controllable magnetism in atomically thin semiconductors,” *Science Advances*, vol. 8, no. 39, p. eabq7650, 2022.

[35] M. Shcherbakov, G. Sartorello, S. Zhang, J. Bocanegra, M. Bosch, M. Tripepi, N. Talisa, A. AlShafey, J. Smith, S. Londo, F. Légaré, E. Chowdhury, and G. Shvets, “Nanoscale reshaping of resonant dielectric microstructures by light-driven explosions,” *Nature Communications*, vol. 14, 10 2023.

[36] C. Wu, N. Arju, G. Kelp, J. A. Fan, J. Dominguez, E. Gonzales, E. Tutuc, I. Brener, and G. Shvets1, “Spectrally selective chiral silicon metasurfaces based on infrared fano resonances,” *Nature Communications*, vol. 5, p. 3892, 2014.

[37] L. Wang, S. Kruk, K. Koshelev, I. Kravchenko, B. Luther-Davies, and Y. Kivshar, “Nonlinear wavefront control with all-dielectric metasurfaces,” *Nano Letters*, vol. 18, no. 6, pp. 3978–3984, 2018.

[38] A. Cicco, P. Giulia, R. Gunnella, Trapananti, Minicucci, R. S. J, C. Daniele, D. M. Lorenzo, P. C. J. Stefano, T. Stefano, and M. Faustino, “Broadband optical ultrafast reflectivity of Si, Ge and GaAs,” *Scientific Reports*, vol. 10, 10 2020.

[39] T. Amotchkina, M. Trubetskoy, D. Hahner, and V. Pervak, “Characterization of e-beam evaporated Ge, YBF<sub>3</sub>, ZnS, and LaF<sub>3</sub> thin films for laser-oriented coatings,” *Applied Optics*, vol. 59, pp. A40–A47, Feb 2020.

[40] I. H. Malitson, “A redetermination of some optical properties of calcium fluoride,” *Applied Optics*, vol. 2, pp. 1103–1107, Nov 1963.

[41] R. Waldron, “Perturbation theory of resonant cavities,” *Proceedings of the IEE - Part C: Monographs*, vol. 107, pp. 272–274, September 1960.

[42] H. A. Bethe and J. Schwinger, “Perturbation theory for cavities,” N.D.R.C. Rpt. D1-117, Cornell University, Ithaca, NY, 1943.

[43] J. Schwinger, “The theory of obstacles in resonant cavities and waveguides,” Tech. Rep. 43-34, Massachusetts Institute of Technology (MIT), Radiation Laboratory, 1943.

[44] W. Hauser, *Introduction to the Principles of Electromagnetism*. Reading, MA: Addison-Wesley, 1971.

[45] D. J. Griffiths and D. F. Schroeter, *Introduction to Quantum Mechanics*. Cambridge: Cambridge University Press, 3 ed., 2018.

[46] J. D. Joannopoulos, S. G. Johnson, J. N. Winn, and R. D. Meade, *Photonic Crystals: Molding the Flow of Light*. Princeton: Princeton University Press, 1995.

[47] S. G. Johnson, M. Ibanescu, M. A. Skorobogatiy, O. Weisberg, J. D. Joannopoulos, and Y. Fink, “Perturbation theory for maxwell’s equations with shifting material boundaries,” *Physical Review E*, vol. 65, p. 066611, Jun 2002.

[48] C. Kottke, A. Farjadpour, and S. G. Johnson, “Perturbation theory for anisotropic dielectric interfaces, and application to subpixel smoothing of discretized numerical methods,” *Physical Review E*, vol. 77, p. 036611, Mar 2008.

[49] S. H. Mousavi, I. Kholmanov, K. B. Alici, D. Purtseladze, N. Arju, K. Tatar, D. Y. Fozdar, J. W. Suk, Y. Hao, A. B. Khanikaev, R. S. Ruoff, and G. Shvets, “Inductive tuning of fano-resonant metasurfaces using plasmonic response of graphene in the mid-infrared,” *Nano Letters*, vol. 13, no. 3, pp. 1111–1117, 2013.

[50] J. C. Slater, “Microwave electronics,” *Reviews of Modern Physics*, vol. 18, pp. 441–512, Oct 1946.

[51] S. Katz, N. Kaplan, and I. Grossinger, “Using diffractive optical elements,” *Laser Technik Journal*, vol. 15, no. 4, pp. 29–32, 2018.

[52] T.-T. Yeh, H. Shirai, C.-M. Tu, T. Fuji, T. Kobayashi, and C. Luo, “Ultrafast carrier dynamics in ge by ultra-broadband mid-infrared probe spectroscopy,” *Scientific Reports*, vol. 7, p. 40492, 01 2017.

[53] J. Van Zeghbroeck, *Principles of Semiconductor Devices*. Boulder: Bart Van Zeghbroeck, 2011.

[54] N. Boroumand, A. Thorpe, A. M. Parks, and T. Brabec, “Keldysh ionization theory of atoms: mathematical details,” *Journal of Physics B: Atomic, Molecular and Optical Physics*, vol. 55, p. 213001, oct 2022.

[55] A. Banos, W. Mori, and J. Dawson, “Computation of the electric and magnetic fields induced in a plasma created by ionization lasting a finite interval of time,” *IEEE Transactions on Plasma Science*, vol. 21, no. 1, pp. 57–69, 1993.

[56] L. Stefanini, D. Ramaccia, M. Barbuto, M. Longhi, A. Monti, S. Vellucci, A. Toscano, A. Alu, V. Galdi, and F. Bilotti, “Time-varying metasurfaces for efficient surface-wave coupling to radiation and frequency conversion,” *Laser & Photonics Reviews*, vol. 18, no. 12, p. 2400315, 2024.

[57] M. R. Shcherbakov, H. Zhang, M. Tripepi, G. Sartorello, N. Talisa, A. AlShafey, Z. Fan, J. Twardowski, L. A. Krivitsky, A. I. Kuznetsov, *et al.*, “Generation of even and odd high harmonics in resonant metasurfaces using single and multiple ultra-intense laser pulses,” *Nature Communications*, vol. 12, no. 1, p. 4185, 2021.

[58] M. J. Mencagli, D. L. Sounas, M. Fink, and N. Engheta, “Static-to-dynamic field conversion with time-varying media,” *Physical Review B*, vol. 105, p. 144301, Apr 2022.

[59] D. R. Austin, K. R. P. Kafka, Y. H. Lai, Z. Wang, C. I. Blaga, and E. A. Chowdhury, “Femtosecond laser damage of germanium from near- to mid-infrared wavelengths,” *Optics Letters*, vol. 43, pp. 3702–3705, Aug 2018.

[60] J. Jackson, *Classical Electrodynamics*. New York: Wiley, 2021.

# Supplementary Online Material for "Generation and Enhancement of Persistent Nanoscale Magnetization in All-Dielectric Metasurfaces by Optically Injected and Localized Free Carriers"

Shivaksh Rawat<sup>\*,1</sup>, Samyobrata Mukherjee<sup>1</sup>, and Gennady Shvets<sup>\*,1</sup>

<sup>1</sup>School of Applied and Engineering Physics, Cornell University, Ithaca, NY 14850, USA

<sup>\*</sup>Email: sr939@cornell.edu, gshvets@cornell.edu

## S1 Predicting Resonance Frequency Shifts

The real unperturbed ( $\mathbf{F}_0$ ) and perturbed ( $\mathbf{F}'$ ) fields inside the resonator are

$$\text{Re}(\mathbf{F}_0) = \mathbf{F}_0(\mathbf{r})e^{-i\omega_0 t} + \text{c.c.}; \quad \text{Re}(\mathbf{F}') = \mathbf{F}'(\mathbf{r})e^{-i\omega t} + \text{c.c.} \quad (1)$$

where  $\mathbf{F}$  represents the complex  $\mathbf{E}$ ,  $\mathbf{D}$ ,  $\mathbf{H}$ , and  $\mathbf{B}$  fields. Here,  $\mathbf{F}_0(\mathbf{r})$  and  $\mathbf{F}'(\mathbf{r})$  are complex field amplitudes which are functions of position. Subtracting the scalar product of Maxwell's curl equation for  $\mathbf{H}'$  with  $\mathbf{E}_0^*$  from the scalar product of the curl equation for  $\mathbf{E}'$  with  $\mathbf{H}_0^*$  yields

$$\mathbf{H}_0^* \cdot (\nabla \times \mathbf{E}') - \mathbf{E}_0^* \cdot (\nabla \times \mathbf{H}') = i\omega \mathbf{B}' \cdot \mathbf{H}_0^* + i\omega \mathbf{D}' \cdot \mathbf{E}_0^*, \quad (2)$$

where  $\omega$  is the perturbed complex resonance frequency and  $'*$  represents the complex conjugate. The LHS of eq. (2) can be rewritten using the divergence formula as[1]

$$\mathbf{H}_0^* \cdot (\nabla \times \mathbf{E}') - \mathbf{E}_0^* \cdot (\nabla \times \mathbf{H}') = \nabla \cdot (\mathbf{E}_0^* \times \mathbf{H}' - \mathbf{H}_0^* \times \mathbf{E}') + \mathbf{E}' \cdot (\nabla \times \mathbf{H}_0^*) - \mathbf{H}' \cdot (\nabla \times \mathbf{E}_0^*) \quad (3)$$

Using the identity in eq. (3) and  $\omega = \omega_0 + \Delta\omega$  (where  $\omega_0$  is the unperturbed complex resonance frequency and  $\Delta\omega$  is the change in resonance frequency due to perturbation) to simplify eq. (2) yields,

$$i\Delta\omega(\mathbf{D}' \cdot \mathbf{E}_0^* + \mathbf{B}' \cdot \mathbf{H}_0^*) = i\omega_0[(\mathbf{D}_0^* \cdot \mathbf{E}' - \mathbf{D}' \cdot \mathbf{E}_0^*) - (\mathbf{B}' \cdot \mathbf{H}_0^* - \mathbf{B}_0^* \cdot \mathbf{H}')] + \nabla \cdot (\mathbf{E}_0^* \times \mathbf{H}' - \mathbf{H}_0^* \times \mathbf{E}') \quad (4)$$

Integrating over the entire volume of the unit cell, we obtain

$$\begin{aligned} \int_V \Delta\omega(\mathbf{D}' \cdot \mathbf{E}_0^* + \mathbf{B}' \cdot \mathbf{H}_0^*) dV &= \int_V \omega_0[(\mathbf{D}_0^* \cdot \mathbf{E}' - \mathbf{D}' \cdot \mathbf{E}_0^*) - (\mathbf{B}' \cdot \mathbf{H}_0^* - \mathbf{B}_0^* \cdot \mathbf{H}')] dV \\ &\quad - i \int_V \nabla \cdot (\mathbf{E}_0^* \times \mathbf{H}' - \mathbf{H}_0^* \times \mathbf{E}') dV \end{aligned} \quad (5)$$

Using Gauss's theorem, the integral with the divergence term (second term on the RHS) in eq. 5 can be rewritten as a surface integral evaluated on the surface  $S$  of the unit cells of the metasurface as

$$-i \int_V \nabla \cdot [\mathbf{E}_0^* \times \mathbf{H}' - \mathbf{H}_0^* \times \mathbf{E}'] dV = -i \oint_S \hat{n} \cdot [\mathbf{E}_0^* \times \mathbf{H}' + \mathbf{E}' \times \mathbf{H}_0^*] dS \quad (6)$$

where  $\hat{n}$  is the unit normal to the surface  $S$ . Furthermore, we assume that the perturbation in the hotspot at the center of the meta atom has negligible impact on the fields at the unit cell walls, so that  $\mathbf{E}'|_{\text{walls}} \approx \mathbf{E}_0|_{\text{walls}}$  and  $\mathbf{H}'|_{\text{walls}} \approx \mathbf{H}_0|_{\text{walls}}$ . Under this assumption, the RHS of eq. 6 may be written as

$$-i \oint_S \hat{n} \cdot [\mathbf{E}_0^* \times \mathbf{H}' + \mathbf{E}' \times \mathbf{H}_0^*] dS \approx -2i \oint_S \hat{n} \cdot \text{Re}(\mathbf{E}_0 \times \mathbf{H}_0^*) dS = -4i \oint_S (\hat{n} \cdot \mathbf{S}_0) dS \quad (7)$$

where  $\mathbf{S}_0$  is the Poynting vector and thus, purely real. Therefore, the surface integral in eq.(7) calculates the change in the imaginary part of the resonance frequency ( $\text{Im}(\Delta\omega)$ ), which is also related to the

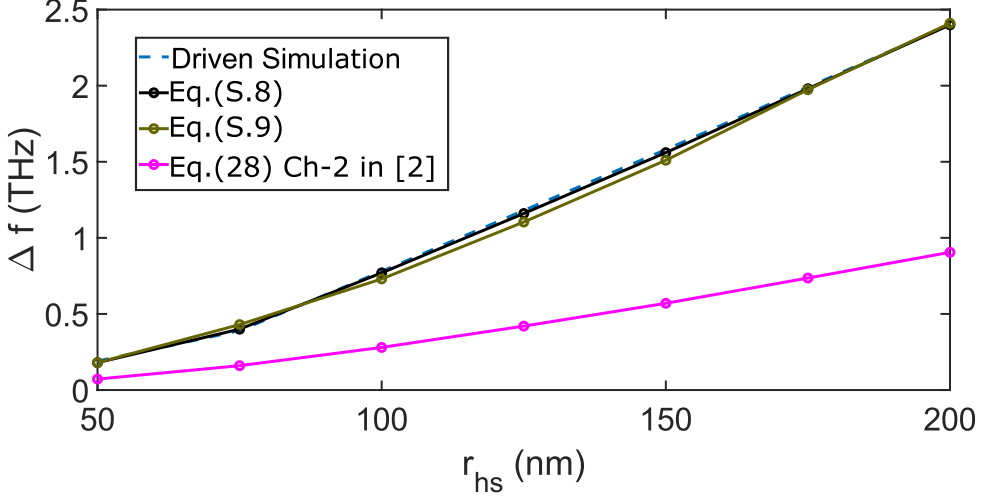


Figure S1: Comparison of the resonance frequency shift predictions.

quality factor of the metasurface resonance. However, since we are only interested in calculating the change in the real part of the resonance frequency ( $\text{Re}(\Delta\omega)$ ), we neglect the surface integral term to obtain

$$\frac{\text{Re}(\Delta\omega)}{\text{Re}(\omega_0)} = \frac{\int_V [(\mathbf{D}_0^* \cdot \mathbf{E}' - \mathbf{D}' \cdot \mathbf{E}_0^*) - (\mathbf{B}' \cdot \mathbf{H}_0^* - \mathbf{B}_0^* \cdot \mathbf{H}')] dV}{\int_V (\mathbf{D}' \cdot \mathbf{E}_0^* + \mathbf{B}' \cdot \mathbf{H}_0^*) dV} \quad (8)$$

However, eq. (8) requires knowledge of the typically unknown perturbed fields to predict the resonance frequency shift. Therefore, we derive an equation that uses only the unperturbed fields and changes in the local permittivity to predict the fractional shifts in resonance frequency (the derivation is shown in Section II.B of the main text).

$$\frac{\text{Re}(\Delta\omega)}{\text{Re}(\omega_0)} = \frac{\text{Re}(\Delta f)}{\text{Re}(f_0)} = \frac{\int_0^{r_{hs}} \left\{ \oint_S \epsilon_0 \left( [\epsilon_{\text{ini}} - \epsilon_{\text{fin}}] |\mathbf{E}_{0\parallel}(\rho)|^2 - \left[ \frac{1}{\epsilon_{\text{ini}}} - \frac{1}{\epsilon_{\text{fin}}} \right] |\mathbf{D}_{0\perp}(\rho)|^2 \right) dS \right\} d\rho}{\int_V (\epsilon_0 \epsilon_{\text{ini}} |\mathbf{E}_0|^2 + \mu_0 |\mathbf{H}_0^2|) dV} \quad (9)$$

The resonance frequency shifts predicted by eq.(8) and eq.(9) are then compared to driven simulations in COMSOL Multiphysics and also with the resonance frequency shifts predicted using eq. (28) in chapter 2 of ref. [2]. Fig. S1 shows the calculated shifts in the metasurface resonance frequency when  $N_e = N_e^{\text{pert}} = 1.6 \times 10^{-19} \text{ cm}^{-3}$  for different hot spot radii ( $r_{hs}$ ) using these various formulae. The shifts predicted by eq. (8), using knowledge of the fields in the perturbed system, are the most accurate and in accordance with the COMSOL simulations. However, we observe that the resonance frequency shifts predicted using eq.(9), using only the unperturbed fields, are reasonably accurate in comparison with eq. (8), and are far more accurate in comparison to the shifts predicted by eq. (28) from chapter 2 of Ref. [2].

## S2 Meta-atom Homogenization: Effective Permittivity Model

In this section, we provide further insight into the behavior of the metasurface resonance upon FC generation, particularly the redshifting of the ED resonance at high values of  $N_e \gtrsim 10^{20} \text{ cm}^{-3}$ . We employ an electrostatic effective capacitor model [3, 4] to homogenize the Ge resonator and the hot spot and calculate its effective permittivity ( $\epsilon_{\text{eff}}$ ). The Ge block and the hot spot are modeled as a parallel plate capacitor, and we calculate the total charge ( $Q$ ) accumulated on the two longer faces ( $\parallel$  to the y-z plane) when a constant potential difference  $V_0$  is applied across them. The capacitor plates have an area  $A = w_y \times h$  with separation  $w_x$  as shown in Fig. S2a. The longer sides of the meta-atom are chosen as the parallel plates of the capacitor in our model because changes in the permittivity of the hot spot located in the center of the Ge block affect  $E_x$  more than  $E_y$ . This can be ascribed to the fact that the maximum (minimum) of  $|E_x|$  ( $|E_y|$ ) coincides with the location of the hot spot, as shown in Fig. S2d(e).

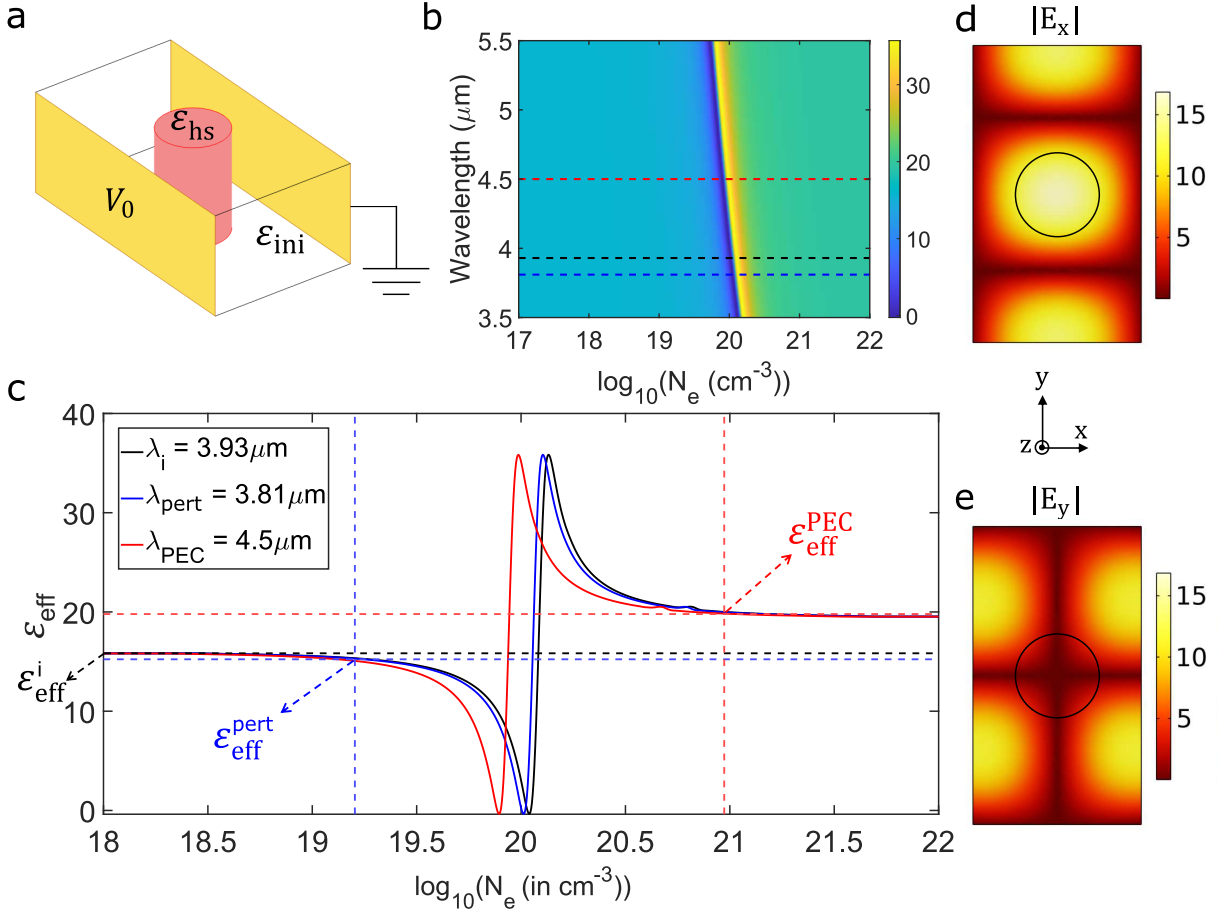


Figure S2: **a.** Geometry for the effective capacitor model. The parallel plates are indicated as golden surfaces and the hot spot in the center in red. **b.** The effective permittivity of the Ge block as a function of local hot spot carrier density and wavelength. The black, blue, and red dashed lines in **c.** represent the  $\lambda_i$ ,  $\lambda_{\text{pert}}$ , and  $\lambda_{\text{PEC}}$  wavelengths, respectively. **c.**  $\epsilon_{\text{eff}}^{\text{xx}}$  as a function of  $N_e$  for three different values of  $\lambda = \lambda_i$  (black),  $\lambda = \lambda_{\text{pert}}$  (blue) and  $\lambda = \lambda_{\text{PEC}}$  (red). **d.**  $|E_x|$  field enhancement in the Ge block with the hot spot region marked using a bold circle. **e.** Same as **d** but for  $|E_y|$ .

Then, after calculating  $Q$ , we obtain  $\epsilon_{\text{eff}}^{\text{xx}}$  for the x-polarized incident light

$$\epsilon_{\text{eff}}^{\text{xx}} = \frac{Q w_x}{\epsilon_0 w_y h V_0}. \quad (10)$$

Fig. S2b shows the value of  $\epsilon_{\text{eff}}^{\text{xx}}$  calculated using the capacitor model for the range of  $N_e$  and  $\lambda$  studied in Fig. 2a of the main text. Fig. S2c shows line cuts of Fig. S2b where we plot the variation in  $\epsilon_{\text{eff}}$  as a function of  $N_e$  for three different wavelengths  $\lambda_i$  (black),  $\lambda_{\text{pert}}$  (blue), and  $\lambda_{\text{PEC}}$  (red). For all the values of  $\lambda$ , we find that at low values of  $N_e$ ,  $\epsilon_{\text{eff}}^{\text{xx}} = \epsilon_{\text{eff}}^i = \epsilon_\infty$ .  $\epsilon_{\text{eff}}^{\text{xx}}$  rapidly decreases from  $\epsilon_\infty$  to 0 for  $10^{19} \text{ cm}^{-3} \lesssim N_e \lesssim 10^{20} \text{ cm}^{-3}$ . For values of  $N_e \gtrsim 10^{20} \text{ cm}^{-3}$ , while the local permittivity of the hot spot becomes negative, the effective permittivity of homogenized medium  $\epsilon_{\text{eff}}^{\text{xx}}$  increases rapidly and saturates at approximately  $\epsilon_{\text{eff}}^{\text{xx}} \approx 20$ . The changes in  $\epsilon_{\text{eff}}^{\text{xx}}$  as  $N_e$  crosses  $\sim 10^{20} \text{ cm}^{-3}$  account for changes in the metasurface resonance wavelength seen in Fig. 2a of the main text as  $N_e$  crosses  $10^{20} \text{ cm}^{-3}$  since the resonance wavelength  $\lambda_r \propto \sqrt{C_{\text{eff}}} \propto \sqrt{\epsilon_{\text{eff}}^{\text{xx}}}$  where  $C_{\text{eff}}$  is the effective capacitance. The intersection of the dashed blue (red) lines shows the value of the effective permittivity for  $\lambda = \lambda_{\text{pert}}$  ( $\lambda_{\text{PEC}}$ ) and  $N_e = N_e^{\text{pert}} (N_e^{\text{PEC}})$ . Thus, localized FC generation in the hot spots initially decreases the effective permittivity of the meta-atom and blue-shifts the metasurface resonance. Further increasing the FC density creates a localized region of high negative permittivity ( $\epsilon_{\text{hs}}$ ) but results in an increase in the effective permittivity and thereby red-shifts the metasurface resonance. Since the effective capacitor model is an electrostatic model, it can only be used to determine the effective permittivity for modifications that primarily modify the electric energy.

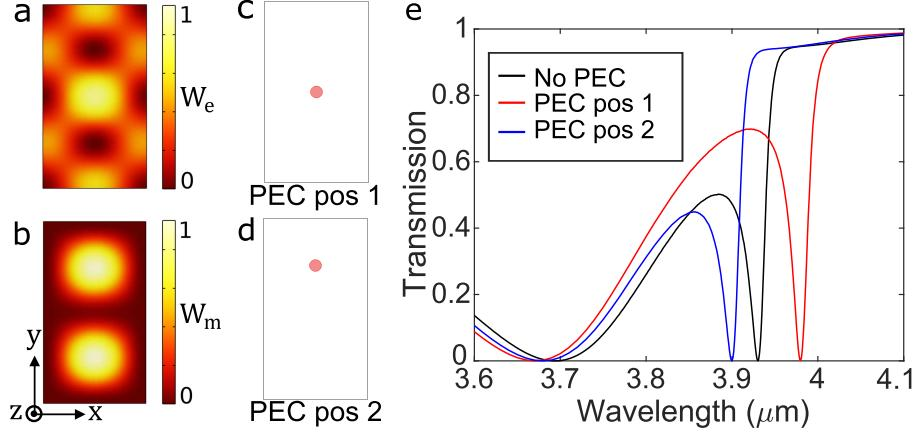


Figure S3: **a.** (b.) Normalized electric (magnetic) energy density of the ED resonance for the unperturbed metasurface. **c.** Schematic showing an effectively metallized (PEC) but smaller hot spot ( $r_{hs} = 50\text{nm}$ ) placed in the center of the Ge block where  $W_e$  is dominant (position 1). **d.** Same as **c** but with the hot spot now placed in a location where  $W_m$  is dominant (position 2). **e.** Metasurface transmission spectrum for the cases where the metasurface is unperturbed (black), PEC is in position 1 (red), and PEC is in position 2 (blue).

### S3 Manipulating Magnetic Energy Density

The electromagnetic energy density of a resonant mode is unevenly distributed within the meta-atom, with the electric and magnetic energy densities dominant in different spatial regions. Therefore, despite considering a metasurface comprising nonmagnetic ( $\mu_r = 1$ ) materials, it is possible to modify the magnetic energy density of the resonant mode, e.g., by effectively metallizing a specific region where the magnetic energy density dominates the electric energy density. According to eq. (5) in the main text, the introduction of a PEC in a region of a resonator where the magnetic (electric) energy density is dominant would result in a blueshift (redshift) of the resonance[5, 6].

Thus, when a strongly metallized (PEC) but smaller hot spot of radius  $r_{hs} = 50\text{ nm}$  is introduced in the center of the Ge block (Fig. S3c), it occupies a region of high electric energy density. This expels the electric field from the PEC volume and increases the effective capacitance while redshifting the ED resonance from  $3.93\text{ }\mu\text{m}$  to  $3.98\text{ }\mu\text{m}$  as shown in Fig. S3e. We have seen this effect in the previous sections, but note that our choice of a smaller hot spot region reduces the extent of the redshift of the ED resonance. However, when a PEC is introduced in an off-center region of the Ge block where the magnetic energy density is dominant (Fig. S3d), the resonance blueshifts to  $3.9\text{ }\mu\text{m}$  (Fig. S3e). Since the PEC now expels the magnetic field, it causes a reduction in the effective inductance of the meta-atom due to excessive FCs shielding the magnetic flux, resulting in a blueshift of the ED resonance.

### S4 Keldysh Model for Required Irradiance Calculation

We used the Keldysh model [7] to determine the time evolution of the FC density ( $N_e(\mathbf{r}, t)$ ) inside the hotspot as a consequence of illumination by a high-intensity, ultra-short pump pulse. We modeled the laser-induced ionization of Ge by combining the photoionization ( $R_{PI}$ ) and avalanche ionization ( $R_{AV}$ ) rates in a single FC density rate equation [8] ,

$$\frac{\partial N_e(\mathbf{r}, t)}{\partial t} = R_{PI}(I[t]) + R_{AV}(I[t])N_e(\mathbf{r}, t) - \frac{N_e(\mathbf{r}, t)}{\tau_{e-h}} \quad (11)$$

where  $I[t]$  is the time-dependent intensity of the pump pulse and  $\tau_{e-h}$  is the electron-hole recombination time. The pump pulse parameters and the material properties of germanium are shown in tabular form below[9, 10, 11].

Parameter	Symbol	Value
Pump wavelength	$\lambda_p$	400 nm
Pulse width	$\tau_p$	8 fs
Band Gap of Ge	$\Delta$	0.8 eV
Reduced effective mass	$m_e$	$0.041 * m_0, m_0 = 9.11 \times 10^{-31} \text{ kg}$
Refractive index (at $\lambda$ )	$n_0$	3
Pump Irradiance	$I[t]$	$I[t] = I_0 e^{-2(t-\tau_2)^2/\tau_p^2}, \tau_2 = 300 \text{ fs}$
e-h Recombination time	$\tau_{e-h}$	100 ps

## S4.1 Photoionization

Photoionization refers to the ionization process in which a photon from a high-intensity laser pulse ejects electrons from a neutral atom, turning it into a charged ion. The photoionization rate calculated using the Keldysh model is given by

$$R_{PI} = 2 \cdot \frac{2\omega}{9\pi} \left( \frac{\sqrt{1+\gamma^2}}{\gamma} \cdot \frac{m_e \omega}{\hbar} \right) \cdot Q_k \left( \gamma, \frac{\Delta_{NP}}{\hbar \omega} \right) \cdot \exp \left[ -\pi \left\langle \frac{\Delta_{NP}}{\hbar \omega} + 1 \right\rangle \cdot \frac{K(\phi) - E(\phi)}{E(\theta)} \right] \quad (12)$$

where a factor of 2 is introduced to account for the electron spin degeneracy and  $Q_k$  represents a slow-varying amplitude function and is written as

$$Q_k(\gamma, x) = \sqrt{\frac{\pi}{2K(\theta)}} \cdot \sum_{n=0}^{+\infty} \exp \left[ -\pi \cdot \frac{K(\phi) - E(\phi)}{E(\theta)} \cdot n \right] \cdot \Phi \left[ \sqrt{\frac{\pi^2(x+1) - x+n}{2K(\theta)E(\theta)}} \right], \quad (13)$$

where,  $K(x)$  and  $E(x)$  are complete elliptic integrals.  $\theta$ ,  $\phi$ , and  $\gamma$  are given as

$$\theta = \frac{1}{1+\gamma^2}, \quad \phi = \frac{\gamma}{1+\gamma^2}, \quad \gamma = \frac{\omega \sqrt{m\Delta}}{eF} \quad (14)$$

$\Phi(x)$  and  $\Delta_{NP}$  represent the Dawson integral and the laser-modified band gap which are given as

$$\Phi(x) = \int_0^x (\chi^2 - x^2) d\chi; \quad \Delta_{NP} = \frac{2}{\pi} \Delta \cdot \left[ \frac{\sqrt{1+\gamma^2}}{\gamma} \cdot E \left( \frac{1}{\sqrt{1+\gamma^2}} \right) \right], \quad (15)$$

where  $\omega = 2\pi c / \lambda_p$  is the angular frequency of the pump pulse,  $e$  is the electronic charge,  $F$  is the local electric field amplitude, and  $\langle x \rangle$  the integer part of  $x$ .

## S4.2 Avalanche Ionization

Avalanche ionization refers to the phenomenon in which a large number of free electrons, accelerated by the intense electric field of the laser, collide with neutral atoms and ionize them, thereby releasing even more free electrons. We calculated the avalanche ionization rate using the single-photon absorption cross section, as the photon at the pump frequency has approximately four times the energy of the direct band gap of Ge ( $hc/\lambda_{pump} \simeq 3.1 \text{ eV} \gg \Delta = 0.8 \text{ eV}$ ). The avalanche ionization rate is given by

$$R_{AV} = \frac{\sigma}{\Delta} I[t] \quad (16)$$

where  $\sigma$  is the single-photon absorption cross section,

$$\sigma = \frac{e^2}{c\epsilon_0 n_0 m_e} \frac{\tau_c}{1 + \omega^2 \tau_c^2}, \quad \tau_c = \frac{16\pi\epsilon_0^2 \sqrt{m_e(0.1\Delta)^3}}{\sqrt{2}e^4 N_e(\mathbf{r}, t)} \quad (17)$$

where  $n_0$  is the invariant component of the refractive index and  $\tau_c$  is the electron relaxation time that depends on the free-electron density.

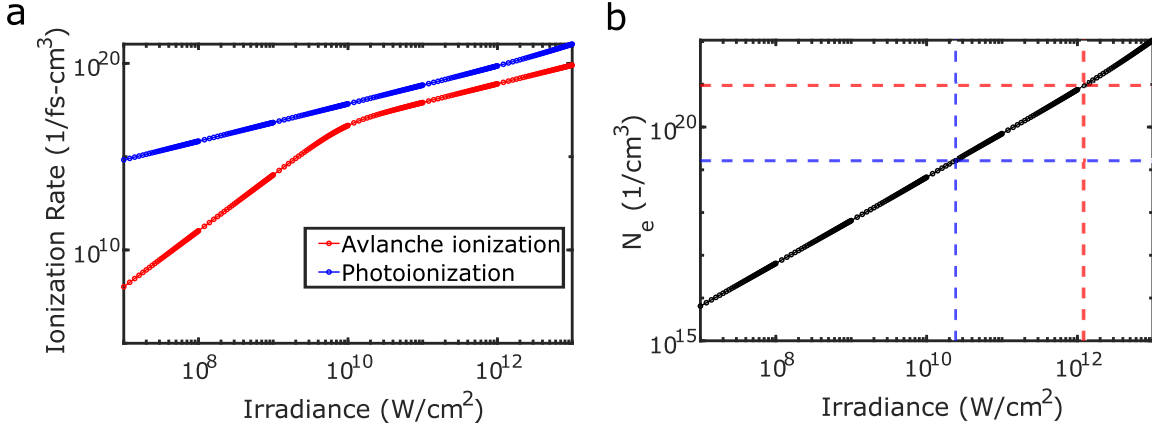


Figure S4: **a.** The photoionization (blue) and avalanche ionization (red) rates for Ge, calculated using the Keldysh model for the given pump pulse parameters. **b.** Carrier concentration ( $N_e$ ) as a function of input irradiance; the red (blue) horizontal and vertical dashed lines represent the carrier concentration  $N_e^{\text{PEC}}$  ( $N_e^{\text{pert}}$ ) and the average irradiance 1.2 TW/cm<sup>2</sup> (24 GW/cm<sup>2</sup>) required for the red-shifting (blue-shifting) of resonance wavelength to  $\lambda_{\text{PEC}}$  ( $\lambda_{\text{pert}}$ ).

### S4.3 Results

The photoionization and avalanche ionization rates in bulk Ge calculated using the Keldysh model for different pump irradiance values are shown in Fig. S4a. Using a source-driven simulation, we observed that the Ge blocks do not exhibit collective behavior at the pump frequency. Therefore, the photoionization and avalanche ionization rates for the Ge blocks are assumed to be the same as the rates for bulk germanium. The free electron concentration in the hotspot for various pump intensities is shown in Fig. S4b. For FC generation in the hotspot  $N_e = N_e^{\text{PEC}}$  (horizontal black dashed line in Fig. S4b, to create the TI shown in Fig. 4b of the main text), an average irradiance of 1.2 TW/cm<sup>2</sup> (vertical red dashed line in Fig. S4b) is required, which corresponds to a peak intensity of 2.15 TW/cm<sup>2</sup>.

## S5 Energy Relations in a Time-Varying Drude-Lorentz Medium

In a time-varying Drude-Lorentz medium, the total electron density  $\mathbf{J}_e$  can be written as the sum of pre-existing free electron density  $\mathbf{J}_e^{(1)}$  and newly created free electron density  $\mathbf{J}_e^{(2)}$  (see eq. (8) and eq. (9) in the main text).

$$\begin{aligned} \mathbf{J}_e(t) &= \frac{\partial \mathbf{P}_e}{\partial t} = \mathbf{J}_e^{(1)}(t) + \mathbf{J}_e^{(2)}(t) = -eN_e^{(1)}\mathbf{v}_e^{(1)}(t) - e \int_{-\infty}^t \frac{\partial N_e^{(2)}}{\partial t'} \mathbf{v}_e^{(2)}(t, t') dt' \\ \mathbf{J}_e^{(1)}(t) &= -\frac{e^2}{m_e} N_e^{(1)} \mathbf{A}(t); \quad \mathbf{J}_e^{(2)}(t) = -\frac{e^2}{m_e} N_e^{(2)} \mathbf{A}(t) + \frac{e^2}{m_e} \int_{-\infty}^t \frac{\partial N_e^{(2)}}{\partial t'} \mathbf{A}(t') dt' \end{aligned} \quad (18)$$

Now, we use Poynting's theorem in conjunction with Maxwell's equations to write the time derivative of the total energy density 'U' in a dispersive medium as [12]

$$\begin{aligned} \frac{\partial U}{\partial t} &= \frac{\partial U_1}{\partial t} + \frac{\partial U_2}{\partial t} = -\nabla \cdot (\mathbf{E} \times \mathbf{H}) = \mathbf{E} \cdot (\nabla \times \mathbf{H}) - \mathbf{H} \cdot (\nabla \times \mathbf{E}) \\ &\Rightarrow \frac{\partial U}{\partial t} = \frac{\partial}{\partial t} \left( \frac{1}{2} \epsilon_0 \epsilon_\infty |\mathbf{E}|^2 + \frac{1}{2} \mu_0 |\mathbf{H}|^2 \right) + \mathbf{E} \cdot \frac{\partial \mathbf{P}_e}{\partial t} \\ U_1 &= \frac{1}{2} \epsilon_0 \epsilon_\infty |\mathbf{E}|^2 + \frac{1}{2} \mu_0 |\mathbf{H}|^2; \quad U_2 = \int_{-\infty}^t \mathbf{E} \cdot \frac{\partial \mathbf{P}_e}{\partial t'} dt' \end{aligned} \quad (19)$$

Using  $\mathbf{E} = -\partial \mathbf{A} / \partial t$ , and from eq. (18), the expression for  $\partial \mathbf{P}_e / \partial t$  in the last term on the right side of eq. (19), we get

$$\mathbf{E} \cdot \frac{\partial \mathbf{P}_e}{\partial t} = -\frac{\partial \mathbf{A}}{\partial t} \cdot (\mathbf{J}_e^{(1)} + \mathbf{J}_e^{(2)}) = \frac{e^2 N_e^{(1)}}{2m_e} \frac{\partial |\mathbf{A}|^2}{\partial t} + \frac{e^2 N_e^{(2)}(t)}{2m_e} \frac{\partial |\mathbf{A}|^2}{\partial t} - \frac{e^2}{m_e} \frac{\partial \mathbf{A}}{\partial t} \cdot \int_{-\infty}^t \frac{\partial N_e^{(2)}}{\partial t'} \mathbf{A}(t') dt' \quad (20)$$

Integrating the equation above and further simplification using integration by parts yields

$$U_2 = \int_{-\infty}^t \mathbf{E} \cdot \frac{\partial \mathbf{P}_e}{\partial t'} dt' = \left[ \frac{e^2 N_e^{(1)} |\mathbf{A}|^2}{2m_e} + \frac{e^2 N_e^{(2)}(t) |\mathbf{A}|^2}{2m_e} - \frac{e^2}{2m_e} \int_{-\infty}^t \frac{\partial N_e^{(2)}}{\partial t'} |\mathbf{A}(t')|^2 dt' \right] - \left[ \mathbf{A}(t) \cdot \int_{-\infty}^t \frac{\partial N_e^{(2)}}{\partial t'} \mathbf{A}(t') dt' - \frac{e^2}{m_e} \int_{-\infty}^t \frac{\partial N_e^{(2)}}{\partial t'} |\mathbf{A}(t')|^2 dt' \right] \quad (21)$$

Further simplifying the above expression,  $U_2$  can be rewritten as

$$U_2 = \frac{1}{2} \epsilon_0 \omega_p^2 |\mathbf{A}|^2 + \int_{-\infty}^t \frac{\partial N_e^{(2)}}{\partial t'} \frac{|e\mathbf{A}(t')|^2}{2m_e} dt' - \mathbf{A}(t) \cdot \left( \frac{e^2}{m_e} \int_{-\infty}^t \frac{\partial N_e^{(2)}}{\partial t'} \mathbf{A}(t') dt' \right) \quad (22)$$

Integrating eq.(19) and using the expressions for  $U_2$  from eq. (22), yields

$$U = \frac{1}{2} \epsilon_0 |\mathbf{E}|^2 + \frac{1}{2} \mu_0 |\mathbf{H}|^2 + \frac{1}{2} \epsilon_0 (\epsilon_\infty - 1) |\mathbf{E}|^2 + \frac{1}{2} \epsilon_0 \omega_p^2 |\mathbf{A}|^2 + \int_{-\infty}^t \frac{\partial N_e^{(2)}}{\partial t'} \frac{|e\mathbf{A}(t')|^2}{2m_e} dt' - \mathbf{A}(t) \cdot \left( \frac{e^2}{m_e} \int_{-\infty}^t \frac{\partial N_e^{(2)}}{\partial t'} \mathbf{A}(t') dt' \right) \quad (23)$$

We use eq. (23) to investigate the effects of a TI on total energy in a Drude-Lorentz medium varying in time where the free electrons that create a TI are generated at rest. A detailed analysis of all the terms in eq. (23) is given in Sections III C and III D of the main text.

## S6 Quasistatic Magnetic Field Amplitude

We use Ampere's law (eq. (12) in the main text) along with the expression for the current density from eq. (18) to write,

$$\nabla(\nabla \cdot \mathbf{A}) - \nabla^2 \mathbf{A} + \frac{\epsilon_\infty}{c^2} \frac{\partial^2 \mathbf{A}}{\partial t^2} + \frac{\omega_p^2}{c^2} \mathbf{A} - \frac{e^2}{\epsilon_0 m_e c^2} \int_{-\infty}^t \frac{\partial N_e^{(2)}}{\partial t'} \mathbf{A}(t') dt' = 0 \quad (24)$$

Now, using Coulomb's Gauge ( $\nabla \cdot \mathbf{A} = 0$ ) and the ansatz suggested in the main text for the magnetic vector potential at a time after the time interface (eq. (13) in the main text for  $t > t_{TI}$ ) yields

$$(\omega_p^2 - \epsilon_\infty \omega_f^2 - c^2 \nabla^2) \mathbf{A}_t + (\omega_p^2 - c^2 \nabla^2) \mathbf{A}_s = \frac{e^2}{\epsilon_0 m_e} \int_{-\infty}^t \frac{\partial N_e^{(2)}}{\partial t'} \mathbf{A}(t') dt' \quad (25)$$

Comparing the time-independent components on the right side of eq. (25) with the left side, we can derive a general differential equation to determine the magnitude of the static magnetic vector potential ( $\mathbf{A}_s$ ) and consequently the static magnetic field ( $\mathbf{H}_s$ ) at the hot spot corresponding to the QS mode as

$$(\omega_p^2 - c^2 \nabla^2) \mathbf{A}_s(\mathbf{r}) = \frac{e^2}{\epsilon_0 m_e} \int_{-\infty}^t \frac{\partial N_e^{(2)}}{\partial t'} \mathbf{A}(\mathbf{r}, t') dt' \quad (26)$$

$$\mathbf{H}_s(\mathbf{r}) = \frac{1}{\mu_0} \nabla \times \mathbf{A}_s(\mathbf{r})$$

Furthermore, we can write the dispersion relation for propagating electromagnetic waves in the hot spot from eq. (25) as

$$\nabla^2 \mathbf{A}_t = \frac{1}{c^2} (\omega_p^2 - \epsilon_\infty \omega_f^2) \mathbf{A}_t \quad (27)$$

For a homogeneous plasma medium, the dispersion relation in eq. (27) for a monochromatic wave propagating with a wave vector  $\mathbf{k}_0$  reduces to the usual dispersion relation of an EM wave in a plasma and gives

$$\epsilon_\infty \omega_f^2 = \omega_p^2 + c^2 \mathbf{k}_0^2 \quad (28)$$

## SOM References

- [1] L. Novotny and B. Hecht, *Principles of Nano-Optics*. Cambridge University Press, 2 ed., 2012.
- [2] J. D. Joannopoulos, S. G. Johnson, J. N. Winn, and R. D. Meade, *Photonic Crystals: Molding the Flow of Light*. Princeton University Press, 1995.
- [3] G. Shvets and Y. A. Urzhumov, “Engineering the electromagnetic properties of periodic nanostructures using electrostatic resonances,” *Phys. Rev. Lett.*, vol. 93, p. 243902, Dec 2004.
- [4] Y. A. Urzhumov and G. Shvets, “Optical magnetism and negative refraction in plasmonic metamaterials,” *Solid State Communications*, vol. 146, no. 5, pp. 208–220, 2008. Special section on Negative Refraction and Metamaterials for Optical Science and Engineering.
- [5] J. C. Slater, “Microwave electronics,” *Rev. Mod. Phys.*, vol. 18, pp. 441–512, Oct 1946.
- [6] T. Ma and G. Shvets, “Scattering-free edge states between heterogeneous photonic topological insulators,” *Phys. Rev. B*, vol. 95, p. 165102, Apr 2017.
- [7] L. V. Keldysh, “Ionization in the Field of a Strong Electromagnetic Wave,” *J. Exp. Theor. Phys.*, vol. 20, no. 5, pp. 1307–1314, 1965.
- [8] V. E. Gruzdev, “Fundamental mechanisms of laser damage of dielectric crystals by ultrashort pulse: ionization dynamics for the Keldysh model,” *Optical Engineering*, vol. 53, no. 12, p. 122515, 2014.
- [9] J. Van Zeghbroeck, *Principles of Semiconductor Devices*. Bart Van Zeghbroeck, 2011.
- [10] T. Amotchkina, M. Trubetskoy, D. Hahner, and V. Pervak, “Characterization of e-beam evaporated ge, ybf<sub>3</sub>, zns, and laf<sub>3</sub> thin films for laser-oriented coatings,” *Appl. Opt.*, vol. 59, pp. A40–A47, Feb 2020.
- [11] T.-T. Yeh, H. Shirai, C.-M. Tu, T. Fuji, T. Kobayashi, and C. Luo, “Ultrafast carrier dynamics in ge by ultra-broadband mid-infrared probe spectroscopy,” *Scientific Reports*, vol. 7, p. 40492, 01 2017.
- [12] L. Landau and E. Lifshitz, *Electrodynamics of Continuous Media*. Course of theoretical physics, Textbook Publishers, 2003.